# **Empirical Formulation for Multiple Groups of Primary Biological Ice Nucleating Particles from Field Observations over Amazonia**

SACHIN PATADE, <sup>a</sup> VAUGHAN T. J. PHILLIPS, <sup>a</sup> PIERRE AMATO, <sup>b</sup> HEINZ G. BINGEMER, <sup>c</sup> SUSANNAH M. BURROWS, <sup>d</sup> PAUL J. DEMOTT, <sup>e</sup> FABIO L. T. GONCALVES, <sup>f</sup> DANIEL A. KNOPF, <sup>g</sup> CINDY E. MORRIS, <sup>h</sup> CARL ALWMARK, <sup>i</sup> PAULO ARTAXO, <sup>j</sup> CHRISTOPHER PÖHLKER, <sup>k</sup> JANN SCHROD, <sup>c</sup> AND BETTINA WEBER<sup>k,l</sup>

(Manuscript received 31 March 2020, in final form 25 March 2021)

ABSTRACT: To resolve the various types of biological ice nuclei (IN) with atmospheric models, an extension of the empirical parameterization (EP) is proposed to predict the active IN from multiple groups of primary biological aerosol particles (PBAPs). Our approach is to utilize coincident observations of PBAP sizes, concentrations, biological composition, and ice nucleating ability. The parameterization organizes PBAPs into five basic groups: 1) fungal spores, 2) bacteria, 3) pollen, 4) viral particles, plant/animal detritus, 5) algae, and their respective fragments. This new biological component of the EP was constructed by fitting predicted concentrations of PBAP IN to those observed at the Amazon Tall Tower Observatory (ATTO) site located in the central Amazon. The fitting parameters for pollen and viral particles and plant/animal detritus, which are much less active as IN than fungal and bacterial groups, are constrained based on their ice nucleation activity from the literature. The parameterization has empirically derived dependencies on the surface area of each group (except algae), and the effects of variability in their mean sizes and number concentrations are represented via their influences on surface area. The concentration of active algal IN is estimated from literature-based measurements. Predictions of this new biological component of the EP are consistent with previous laboratory and field observations not used in its construction. The EP scheme was implemented in a 0D parcel model. It confirms that biological IN account for most of the total IN activation at temperatures warmer than  $-20^{\circ}$ C and at colder temperatures dust and soot become increasingly more important to ice nucleation.

KEYWORDS: Aerosols; Cloud microphysics; Cloud parameterizations; Parameterization

### 1. Introduction

Often referred to as bioaerosols, primary biological aerosol particles (PBAPs) are a subset of biogenic particles emitted from Earth's surface. They consist of biological material such as viruses, algae, bacteria, fungal spores, pollen, plant and animal detritus, and their fragments and secretions. In the ambient atmosphere, bioaerosols may be present in the form of clusters, single particles, and agglomerates and exist in a variety of shapes such as rods, spirals, spherical, or spheroidal forms. A review article by Després et al. (2012) describes typical concentrations of these PBAPs in the ambient air, their sizes, and sampling techniques. Bioaerosols can act as ice nuclei (IN) to initiate ice at temperatures often warmer than  $-12^{\circ}$ C, well

Corresponding author: Dr. Sachin Patade, sachin.patade@nateko.lu.se

above the homogeneous freezing point (Prenni et al. 2009; DeMott and Prenni 2010; Morris et al. 2013; Fröhlich-Nowoisky et al. 2016). To maintain consistency with previous EP papers (e.g., for mathematical symbols), we will use the term "IN" rather than "ice nucleating particles" (INPs; Vali et al. 2015) for this paper. PBAPs can also act as giant cloud condensation nuclei (CCN) (Barahona et al. 2010; Delort et al. 2010), and may play an important role in the hydrological cycle. Bioaerosols may influence the formation of precipitation, especially in pristine air over densely vegetated areas (Phillips et al. 2009; Pöschl et al. 2010; Huffman et al. 2013; Prenni et al. 2013).

In warm-based convective clouds, rain production can occur through collision-coalescence ("warm rain process"). Heterogeneous nucleation of ice crystals and their subsequent growth to form snow and graupel particles ("ice crystal process") plays an essential role in rain formation in convective

clouds with colder cloud bases (e.g., Rogers and Yau 1989; Pruppacher and Klett 1997). The role of bioaerosols in altering cloud microphysical properties, precipitation, and ecosystem interactions has been recognized for many years and is a topic of increasing interest (e.g., Pöschl et al. 2010; Huffman et al. 2013; Amato et al. 2015). The PBAPs can play an essential role in altering both warm and cold rain processes by acting as CCN and IN (Phillips et al. 2009). However, large uncertainty still exists regarding their potential to facilitate precipitation, particularly their impact on global or on regional scales (Hoose et al. 2010; Morris et al. 2011).

As reviewed by Després et al. (2012), several previously published studies have reported ice nucleation activities of various biological species, including fungi, pollen, algae, and bacteria. Among various PBAP species, higher ice nucleation activity is observed for bacterial and fungal particles in clouds. Quantitative measurements of biological IN in the atmosphere are rare. Biological IN in the atmosphere exhibit strong temporal and spatial variations (Christner et al. 2008; Pouzet et al. 2017). For a better understanding of their impact on clouds, more quantitative measurements of biological IN in Earth's atmosphere are required.

Even with only limited observations of biological IN, numerical models can serve as an important tool for investigating their effect on cloud microphysical processes and hence on precipitation. Using a 1.5-dimensional cloud model, Levin et al. (1987) studied the efficiency of cloud seeding with bacteria. Ariya et al. (2009) showed that biological IN could trigger cloud glaciation through ice multiplication processes. Diehl and Mitra (2015) implemented PBAPs (pollen and bacteria) in a parcel model using the ice-active mass site density approach (Kanji et al. 2017, and references therein) and found that these PBAPs were not involved in significant ice formation. Hummel et al. (2018) implemented PBAPs in the regional atmospheric model. They showed that although PBAPs were very efficient IN at high subzero temperatures, due to their low atmospheric concentrations, it is difficult to quantify their impact on cloud properties. However, they also showed that PBAPs could influence the phase of clouds with ice at temperatures below -15°C in the absence of any other IN. Hiron and Flossmann (2015) studied the potential impact from bacteria as extremely IN active PBAP on cloud and rain development. They noticed a significant increase in rainfall flux in the simulation with only bacteria as IN. However, in simulations where all other IN modes were also forming ice, the influence on rainfall became negligible.

For mesoscale systems of warm-based deep convection over the United States, Phillips et al. (2009) showed that an increase in PBAP loading resulted in more numerous cloud droplets through their CCN activity and reduced precipitation production via the warm rain process, boosting the lifetime and extent of clouds. In the case of higher loadings of bioaerosol, the extra heterogeneous ice from biological IN particles can only partially counteract that effect, indicating that the CCN activity of PBAPs was more important than their IN activity for the simulated warm-based convection.

Equally, several studies have used regional as well as global models to understand the geographical variation and climatic importance of bioaerosols (e.g., Burrows et al. 2009a; Hoose et al. 2010; Sesartic et al. 2012). The empirical data included in these models are highly uncertain. Most of the current parameterizations of heterogeneous ice nucleation of biological particles are based on laboratory measurements or are derived from theory.

In view of such uncertainty, cloud-resolving numerical models need to be constrained and validated by using observational data of biological IN so as to acquire a better estimation of their effect on clouds. Arguably, using a "bottom-up approach" (i.e., measurements of ice nucleation activity of biological species in the laboratory to represent atmospheric ice initiation) in the numerical models might introduce significant bias in the active IN concentrations because the particular biological species studied in the laboratory may not necessarily be representative of the real PBAP populations of diverse composition in the atmosphere. Instead, there is a need for an improved parameterization of heterogeneous ice nucleation of biological IN that represents the effects arising from the diversity of their physical and chemical characteristics in nature. We have followed a "topdown" approach in the current study to resolve the ice nucleation activity of multiple groups of PBAPs collected directly from the atmosphere.

The empirical parameterization (EP) for heterogeneous ice nucleation presented here is based on the approach of quantifying the active surface site density (e.g., Phillips et al. 2008; Niemand et al. 2012; Kanji et al. 2017, and references therein). The assumption of active surface site density has some limitations related to the need to describe consistently the freezing curves over a wide range of surface areas, as described in Beydoun et al. (2016). The first empirical ice nucleation parameterization for biological particles was proposed by Phillips et al. (2008), where biological particles were assigned as a part of insoluble organic particles. An estimation of the number of active IN consisting of insoluble aerosol species assumed that it was approximately proportional to the total surface area of its aerosol particles. In the subsequent study, Phillips et al. (2013) revised the original EP scheme by replacing insoluble aerosol species by the new group specifically for PBAP IN. However, that version of the scheme did not address the separate activities of various groups of PBAPs with different ice nucleating abilities.

In the present study, a framework for parameterizing the heterogeneous ice nucleation of biological particles is formulated and accounts for contributions from various groups of PBAPs including

- 1) fungal spores and associated fragments;
- 2) bacteria and their fragments;
- 3) pollen and their fragments;
- 4) viral, plant/animal detritus; and
- 5) algae.

Matthias-Maser and Jaenicke (1995) first described these groups of PBAPs through microscopy observations of natural samples from the real atmosphere. As with past versions of

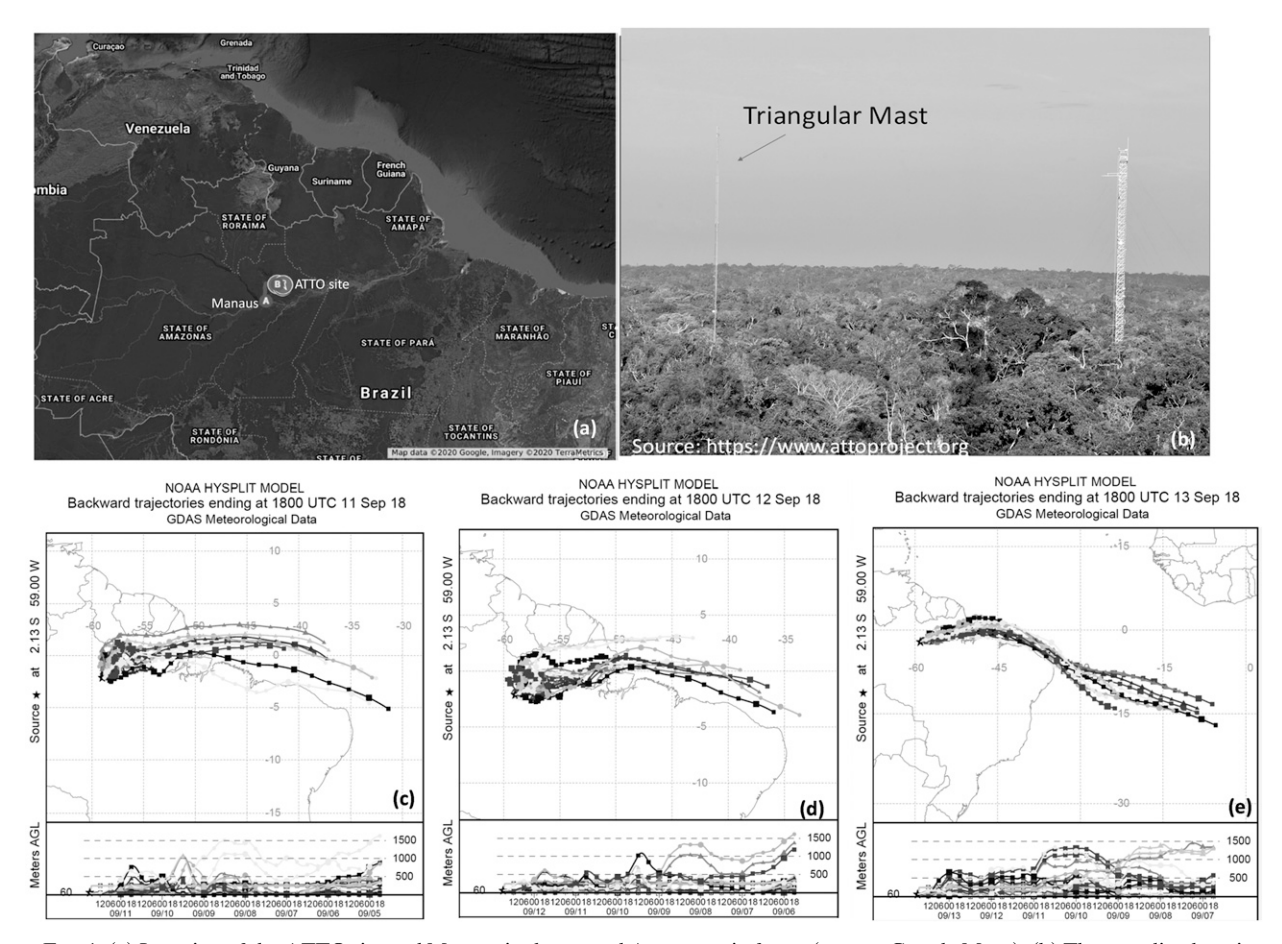


FIG. 1. (a) Location of the ATTO site and Manaus in the central Amazon rain forest (source: Google Maps). (b) The sampling location at the ATTO site includes a triangular mast on which a total suspended particles (TSP) inlet was installed at 60 m above ground. (c)–(e) The HYSPLIT 7-day (168 h) ensemble backward trajectories for three typical sampling days (11–13 Sep 2018) are shown for an endpoint altitude of 60 m.

the EP, our proposed treatment applies to all known modes of heterogeneous ice nucleation including deposition, and condensation/immersion-freezing modes. For contact freezing, the approach followed by Phillips et al. (2008) is adopted (see appendix E).

The proposed scheme is empirical, mostly based on coincident observations of PBAP size distributions and active biological IN sampled from the atmosphere over the Amazon rain forest with abundant PBAPs. Prenni et al. (2009) have observed that over the Amazon rain forest the activity of biological IN (a few per liter) dominates all ice nucleation at temperatures warmer than  $-25^{\circ}$ C, whereas the contribution of dust particles prevails at colder temperatures. Hence, this region is ideal for biological IN measurements.

#### 2. Material and methods

### a. Measurement site

Samples for the present study were collected over the central Amazon basin at the Amazon Tall Tower Observatory

(ATTO; Andreae et al. 2015). The ATTO site is in the middle of the Amazon rain forest in northern Brazil (see Fig. 1), about 150 km northeast of Manaus (120 m above sea level) with coordinates 2°08′45.13″S 59°00′20.12″W. The measurement facilities at the ATTO site consist of a 325 m tall tower and two 80 m towers, one of which is a triangular mast currently used for a wide range of aerosol measurements (Andreae et al. 2015). The immediate surroundings, as well as the ATTO footprint region, are covered by an old-growth undisturbed forest where there is minimal anthropogenic impact.

Meteorological conditions vary throughout the year with wet (February–May) and dry (August–November) seasons and a transition from wet to dry season in between (December–January) (Pöhlker et al. 2019). This classification of seasons is consistent with the seasonality of atmospheric pollution, rainfall, and air mass origin. Over the Amazon rain forest, PBAPs are ubiquitous throughout the year (Martin et al. 2010). During the wet season, the atmospheric boundary layer over the Amazon is relatively clean with low number concentrations of aerosols (Artaxo et al. 2002; Martin et al. 2010). The hydrological cycle is strongly influenced by biogenic aerosols in

particular. However, during the Amazonian dry season, atmospheric aerosol concentrations are considerably higher due to biomass burning (Andreae et al. 1988; Artaxo et al. 2002; Pöhlker et al. 2018; Holanda et al. 2020) and mixed-pollution scenarios (Pöhlker et al. 2018). A detailed description of the aerosol size distribution and CCN characteristics at the ATTO site are given by Pöhlker et al. (2016, 2018). Additional details on the diurnal temperature and wind variations, precipitation amounts, and aerosol characteristics at the ATTO site are from Andreae et al. (2015).

Sampling was performed during the dry season in the Amazon between 5 and 18 September 2018. Collection of samples was interrupted on a few days, including 9 and 15 September due to damage to a power supply, so sample collection was only possible for 12 days (see Fig. 5a). As shown in Fig. 1, sampling took place at the triangular mast site. Sampled air was carried through a stainless-steel tubing with a diameter of 0.75 in. to the aerosol sampling unit installed in a laboratory container located at the base of a triangular mast. A total suspended particles (TSP) inlet was installed on a triangular mast at 60 m above ground level to ensure that air was sampled from above the canopy, which has an average height of  $\sim$ 23 m. The sampled air from the TSP inlet was dried to a relative humidity < 40% using silica gel driers to avoid condensation in the filter holder.

The inlet used for sample collection in the current study has been optimized to achieve a maximum sampling efficiency (Moran-Zuloaga et al. 2018); however, a certain amount of particle loss is unavoidable. Particles smaller than 100 nm are more prone to diffusive losses and not relevant for the current study. Moran-Zuloaga et al. (2018) documented potential losses in the accumulation and coarse mode particles of aerosol particles in this inlet system, which are more relevant to the current study. They calculated the transmission efficiencies of PBAPs for the inlet used in the current study by using a standard density of 1 g cm<sup>-3</sup> as the best guess for typical PBAP densities. The aerosol transmission efficiency starts at about 100% (full transmission) for particles with a diameter of 0.7  $\mu$ m and then declines with increasing particle size. Based on their calculation, typical transmission efficiencies for PBAPs with diameter 1, 2, 4, 8, and  $10 \mu m$  were 98%, 97%, 91%, 72%, and 55%, respectively. Corrections to PBAP size distributions were applied accordingly.

A detailed analysis of the back trajectories arriving at the ATTO site is presented in Moran-Zuloaga et al. (2018) and Pöhlker et al. (2019). They showed that the ATTO-relevant back trajectories followed a seasonal swing between a northeast path during the wet season and a southeast path during the dry season as a response to the annual north-south migration of the intertropical convergence zone. Figure 1 shows the 7-day analysis from the Hybrid Single-Particle Lagrangian Integrated Trajectory model (Draxler and Rolph 2003) on three sampling days (11–13 September 2018) at 60 m above ground. Back trajectories revealed that the anthropogenic emissions from Manaus did not significantly impact the sampled air mass; however, the atmospheric conditions at the ATTO site during our sampling period were not pristine.

### b. Aerosol measurements and sample collection

#### 1) AEROSOL SIZE DISTRIBUTION MEASUREMENTS

The aerosol size distribution and number concentration at the ATTO site were measured by a Scanning Mobility Particle Sizer (SMPS; TSI Inc.) and an Aerodynamic Particle Sizer (APS; TSI Inc.). The SMPS measures the electrical mobility diameter (10–430 nm), while the APS gives aerodynamic diameters (0.5–20  $\mu m$ ) of the particles. There were frequent interruptions in aerosol measurements during our observational period due to lightning strikes and associated damage to the power supply and installation. Therefore, simultaneous measurements of the aerosol size distribution from both the SMPS and APS were available only for a few days.

#### 2) AEROSOL COLLECTION BY FILTER METHOD

Table 1 describes the sampling type, duration, flow rate, purpose, and corresponding instrument in which the samples were analyzed. The aerosol samples were collected from 5 to 18 September 2018, for a 12-day period at the ATTO site. The collection of aerosol samples for the drop freezing tests and microscopic analysis was carried out via the TSP inlet through a four-stage stacked filter unit. Four polytetrafluoroethylene (PTFE) membrane filter papers (25 mm diameter; Sartorius Stedim Biotech) with the pore sizes of 5 (outermost), 1.2, 0.45, and 0.2 (innermost)  $\mu$ m were used for the sampling. The filters were placed in an airtight aluminum filter holder in order of decreasing pore size. Samples were collected with a vacuum pump (VWR vacuum gas PM20405-86). The flow rate was controlled using a flowmeter (Kytola Instruments) equipped with a needle valve. Collection efficiencies of PTFE membrane filters of pore size 5 and 1.2 μm are much higher compared to Millipore and glass filters of similar pore sizes (Soo et al. 2016). Thus, inevitably most of the aerosol particles are collected on the first two filters.

Cascade filter samples were collected with an average volumetric sample flow rate of  $4 \, L \, min^{-1}$  for approximately  $4 \, h$  each day. In addition, a set of cascade filters with a sample flow rate of  $1.5 \, L \, min^{-1}$  was collected for about  $16 \, h$ . A set of aerosol samples with a sample volume of about  $200 \, L$  was collected using only a  $0.2 \, \mu m$  filter to estimate IN concentrations activated by the immersion-freezing mode in Frankfurt Ice Nuclei Deposition Experiment (FRIDGE-IMM) chamber.

Samples were sealed carefully in a sterile container and stored at 4°C at the ATTO site and during the transportation. After the campaign was completed, the samples were transported to the University of Sao Paulo and later to Lund (Sweden). The samples were stored in a deep freezer at  $-25^{\circ}$ C at Lund until they were analyzed by scanning electron microscopy (SEM) and drop freezing tests.

Aerosol samples, when stored for a prolonged time at warm temperatures (e.g., above  $0^{\circ}$ C), can show changes in their ice nucleation activity. Stopelli et al. (2014) found a degradation in the active IN concentration by a factor of 2 ( $-8^{\circ}$  to  $-12^{\circ}$ C) in snow water samples stored at  $4^{\circ}$ C for 30 days. We were unable to store samples at temperatures as cold as  $-25^{\circ}$ C immediately after collection as it was technically not possible to transport the aerosol samples stored at such freezing temperatures. Any

TABLE 1. Daily sampling plan along with sampling type, time duration, flow rate, volume sampled, sampling purpose, and the instrument used for sample analysis.

Type of aerosol sampling	Time (UTC)	Flow rate (sample volume)	Purpose	Instrument used in the analysis
0.2 μm filter only	1400-1450	4 L min <sup>-1</sup> (200 L)	Immersion freezing IN	FRIDGE-IMM
PEAC7	1500–1550	$2 \mathrm{L}\mathrm{min}^{-1} (100 \mathrm{L})$	Deposition and condensation- freezing IN, SEM	FRIDGE-STD, SEM
Cascading filtering, day	1600–2010	$4 \mathrm{Lmin}^{-1} (1000 \mathrm{L})$	SEM, biological IN	LINDA, SEM, flow cytometry
Cascading filtering, overnight	2030–1230 (next day)	$1.5 \mathrm{Lmin^{-1}} (1440 \mathrm{L})$	SEM, biological IN	LINDA, SEM, flow cytometry

samples, stored first at a colder temperature and then subjected to warm temperatures, could develop condensation on the filter, which would not be ideal for biological samples.

### 3) AEROSOL COLLECTION BY PEAC7

In addition to the filter method, aerosol sampling was performed using a Programmable Electrostatic Aerosol collector (PEAC7) (Schrod et al. 2016). The PEAC7 samples were analyzed to estimate IN activated by deposition and condensation-freezing modes in the FRIDGE-STD chamber. A total of 12 samples were collected using PEAC7 during the field campaign held from 5 to 18 September 2018 (see Fig. 5).

In addition, PEAC7 samples were used for imaging PBAPs by SEM. On each sampling day, aerosol particles were collected at a volumetric flow rate of  $2 \, \mathrm{L\,min^{-1}}$  using the PEAC7 for 50 min. The PEAC7 unit used in the current analysis is based on the single wafer electrostatic aerosol collector described in Klein et al. (2010). In PEAC7, aerosol particles are introduced through a central inlet into the field of electrons emitted by 12 gold electrodes. The aerosols are negatively charged and carried to the positively charged silicon (Si) wafers (Wacker-Siltronic, thickness: 0.7 mm; diameter: 45 mm) where they are deposited onto the surface (Klein et al. 2010).

We have applied a correction to the IN concentrations and size distribution of bioaerosol particles measured by the PEAC7 by assuming a collection efficiency of 60% for deposition onto each wafer, as observed by Schrod et al. (2016). Klein et al. (2010) and Schrod et al. (2016) provide additional details on the design and working principle of PEAC7.

### c. Scanning electron microscopy analysis

Primary bioaerosol particles were analyzed by using a variable pressure Tescan Mira3 High-Resolution Schottky FE-SEM located in the geology department at Lund University. It should be noted that the SEM analysis was limited to three days: 9 (nighttime; hereafter 0911N), 12 (daytime; hereafter 0912D), and 13 (daytime; hereafter 0913D) September, as an intensive collection of SEM images characterizing the size distributions for all the samples was not practical. During each of the three days, the size distribution and IN number were estimated for total biological aerosols (both 5 and 1.2  $\mu$ m filters combined) and fractions obtained on each of the 5 and 1.2  $\mu$ m filters separately. Thus, nine pairs of measurements of active

IN and size distributions were available from three intensive sampling days mentioned above and will be referred to as the nine "cases" hereafter.

The samples were coated with a thin layer (10 nm) of palladium, sputter deposited prior to the SEM analysis, to reduce charging under the electron beam. The coated samples were examined at a beam size of 15 keV with a working distance of 10 mm. The working distance was lowered (between 5 and 10 mm) for Si wafer samples to obtain clearer images of particles with a diameter  $D < 1.5 \,\mu m$ .

The organic nature of particles from energy-dispersive X-ray spectrometer (EDS) analysis was confirmed if (C + O) > 75% and 1% < P, K, Cl < 10% (Coz et al. 2010). The SEM system used in the current study was equipped with an energy-dispersive X-ray spectrometer (EDS, X-Max<sup>N</sup> 80, Oxford Instruments, 124 eV, 80 mm<sup>2</sup>). The EDS could detect the composition of individual particles semiquantitatively for elements with an atomic number greater than six including light elements such as C, N, and O. Errors in measurements of the composition of light elements by EDS vary for individual samples and are below 2% overall. The EDS was performed at a beam intensity of 15 keV with a working distance of 10 mm. The Si and F peaks in the EDS spectra were not considered for particles from the Si wafer and PTFE filter, respectively, because of interference from the substrate. The duration of each EDS collection was limited to 10–12 s to avoid particle damage. Because other elements like S, Ca, or Si can also be regarded as tracers of PBAPs, this analysis should be treated as a conservative estimate.

Before imaging the individual biological particles, wide reference areas each  $100\,\mu\mathrm{m} \times 100\,\mu\mathrm{m}$  in size were chosen randomly. Corresponding images of those areas were saved as reference pictures along with their positions on the filter paper. Particles located in these predefined reference spots were counted, and high-resolution images were acquired for those particles. About five particles were observed roughly at each predefined reference spots on the filter samples. The maximum dimension of particles was recorded and saved. In this study, the maximum dimension is treated as the diameter of the particle.

Based on the number of PBAPs detected in the scanned filter area, the bioaerosol number was upscaled to the whole filter area. The size distribution of the PBAPs was classified

into 40 predefined size bins covering a size range from 0.2 to  $40 \,\mu\text{m}$ . The measured number was converted to an airborne concentration (m<sup>-3</sup> of air) based on the sampled air volume. The recorded data were then used to classify particles into the basic PBAP groups: fungal spores, bacteria, pollen, viral particles, plant/animal detritus, algae, and their respective fragments. The primary classification of PBAPs among various groups was based on similarity in morphological characteristics with those reported in earlier studies. Despite all possible efforts to categorize the identified PBAPs, not all of them could be attributed to any PBAP group. A small fraction of the PBAPs (~5%) which did not find any similarity in morphology with the PBAP groups considered here were classified as "unidentified" PBAPs. These unidentified particles were not included in the size distributions of PBAPs presented here.

Since the emphasis of the current study was to characterize the size distributions of PBAPs, nonbiological particles were excluded from the study. In addition to filter samples, Si wafers were analyzed by SEM using a similar methodology. Additional details about SEM analysis, including scanned area and numbers of bioaerosol images collected, are given in Table 2. More than 0.1% of the total filter area was investigated under SEM, and >200 images were collected for each sampling day considered for SEM analysis. For Si wafers, more than 0.06% of the total area was scanned under SEM, and ~100 images of PBAPs were collected.

It was challenging to identify and count particles with a  $D < 1.5 \,\mu\text{m}$  (e.g., bacteria) on filter samples because they were often hidden inside the dense filter material membrane. Therefore, the size distribution of biological particles with  $D < 1.5 \,\mu \text{m}$  were determined mostly by SEM imaging of Si wafers. This was justified as the size distributions from the Si wafer, and the corresponding filter were in good agreement within the overlapping region between 1.5 and 5  $\mu$ m. The collection efficiency of the 5  $\mu$ m filter for various particle diameters was estimated based on total aerosol number concentrations from the SMPS, APS, and the size distribution of total particles collected on the 1.2  $\mu$ m filter. The SMPS and APS aerosol size distributions used here were from 14 September, a typical sampling day at the ATTO site. Based on the collection efficiency of the 5  $\mu$ m filter, the size distributions of biological particles on 5 and  $1.2 \,\mu m$  filters were estimated separately. The estimated collection efficiency for particles with a diameter between 0.3 and 6 µm was variable between 0.81 and 0.99, whereas it was unity for other size ranges. The collection efficiency of  $1.2 \,\mu \text{m}$  filters was not measured and assumed to be unity (for particles with  $D > 0.1 \,\mu\text{m}$ ) based on measurements by Soo et al. (2016).

After acquiring the images of bioaerosols from SEM analysis, we classified them into common PBAP groups based on size and morphology.

### d. Flow cytometry analysis

In addition to SEM, we conducted flow cytometry (FCM) analysis to estimate the total bioaerosol number concentration. FCM is widely used to detect and measure the physical

TABLE 2. Details of SEM analysis including sample volume, scanned area, and the number of bioaerosol images collected for filters. The values for Si wafers are given in parentheses.

Sample	Sample volume (L)	Scanned area (%)	Total images
0911N	1500 (100)	0.14 (0.064)	302 (101)
0912D	1000 (100)	0.1 (0.062)	201 (114)
0913D	100 (100)	0.11 (0.07)	210 (103)

and chemical characteristics of cells or particles. This is a fluorescence technique, in which cells are often labeled with fluorescent markers so that light is absorbed and then emitted in a wavelength band. For each sample extract, cell counts were performed on 450  $\mu$ L triplicates added with 50  $\mu$ L 5% glutaraldehyde (stored at 4°C). For analysis, sample extracts were stained with SYBRGreen I (Molecular Probes Inc.). This stains nucleic acids, and thus reveals all DNA-containing particulate matter (e.g., viruses, bacteria, archaea, fungi, pollen, and plant and animal cells). The parameters used with FCM did not detect chlorophyll, proteins, and carotenoids. The wavelengths for excitation and emission were 488 and 530 nm, respectively. The FCM counts were performed for 3 min. The flow cytometry technique used in the current analysis can detect particles as small as 0.3  $\mu$ m (Lippé 2018).

### e. Measurement of ice nucleating particles

IN in the air were measured using the FRIDGE chamber of Goethe University, Frankfurt. FRIDGE operates in two different modes: 1) as a low-pressure diffusion chamber (here called FRIDGE-STD) for the detection of deposition/condensation freezing IN collected onto Si wafers [section 2b(3)], and 2) as a cold-stage freezing array (here called FRIDGE-IMM) for the measurement of immersion freezing IN in extracts of filter samples [section 2b(2)]. Additional details have been described in previous studies (Klein et al. 2010; Schrod et al. 2016; DeMott et al. 2018).

# 1) MEASUREMENT OF IN ACTIVATED BY DEPOSITION AND CONDENSATION FREEING MODE USING FRIDGE-STD

The FRIDGE-STD method applies a static low-pressure diffusion chamber for activation, growth and counting of IN activated at temperatures between 0° and -30°C. For analysis, a Si wafer substrate that was previously laden with electrostatically precipitated aerosol particles (using PEAC7) was placed on the cold stage in the chamber. The chamber was then closed, evacuated, and cooled to the desired temperature. The surface temperature was measured using a PT-1000 sensor. In the next step, water vapor was introduced into the chamber by opening the connection to the vapor source. The supersaturation with respect to ice over the Si wafer was then estimated as the ratio of vapor pressure in the chamber over saturation vapor pressure at the surface temperature. The number of activated ice crystals grown was counted using automatic picture analysis software. All of the 12 samples collected on Si wafer by PEAC7 were processed for IN activation in the FRIDGE-STD mode (Figs. 5a-c).

# 2) MEASUREMENT OF IN ACTIVATED BY IMMERSION FREEZING MODE USING FRIDGE-IMM

Number concentrations of IN in the air, activated by immersion freezing mode, were measured on the cold stage of FRIDGE-IMM with the drop freezing method of Vali (1971), as described by Ardon-Dryer and Levin (2014) and DeMott et al. (2018). The aerosol samples collected on  $0.2 \,\mu m$  filters were used for the drop freezing experiment. Each filter was placed in 5 mL of deionized water and stirred vigorously for a few minutes to create particle suspensions. Around 60 droplets, each with a volume of 2.5 µL were pipetted onto a clean, salinized Si wafer, with the chamber almost closed, but at ambient atmospheric pressure. The temperature of the cold stage was lowered by 1°C min<sup>-1</sup>. A steady flow of synthetic air of  $1 \,\mathrm{L}\,\mathrm{min}^{-1}$  through the chamber avoided any condensation and rime effects. The number of drops that froze as a function of temperature was recorded by the charge-coupled device (CCD) camera. Two runs of drop freezing experiments were conducted for each sample. In FRIDGE-IMM, 11 filter samples were treated to measure the IN concentrations activated by immersion freezing mode (see Fig. 5d).

### 3) QUANTIFICATION OF BIOLOGICAL IN

The concentration of biological IN in the air, active between -5° and -15°C, was determined by conducting the drop freezing experiments in the LED-Based Ice Nucleation Detection Apparatus (LINDA) chamber as described below. The detailed technical information and working principle of LINDA are described by Stopelli et al. (2014) and summarized here. The LINDA device has an array  $(7 \times 8)$  of red light emitting diodes (LEDs; 645 nm wavelength). This array is mounted on a printed circuit board cast into a polycarbonate housing and submersed in a cold bath. A liquid sample is distributed in a total of 52 sample tubes (0.5 mL Eppendorf). These tubes are held in another polycarbonate plate and placed onto the LED array so that each tube is located above one LED. The temperature is recorded by four sample tubes with cast-in Pt-1000 temperature sensors placed in the corner positions of the tube holder.

Before starting the freezing experiment, 75% of each filter sample was placed in 30 mL of deionized water to create suspensions, of which 20 mL was used for the freezing experiment in LINDA. The remaining 25% of the filter was saved and stored in a petri dish for SEM analysis. The filter samples were cut using a sterilized scalpel. A small amount of (2 mL) NaCl (in liquid form, 0.8% w/v) was added to the solution to make the LINDA sample extract clearer to facilitate the imaging. Adding NaCl to the LINDA sample extracts cannot have affected its freezing characteristics since no freezing event was noticed for the solution containing deionized water and NaCl. The remaining 10 mL solution was saved and stored in a refrigerator (at 4°C) for subsequent flow cytometry.

The sample extract was distributed in a total of 52 sample tubes, each of which contains  $400 \,\mu\text{L}$  of the sample extract. The samples were analyzed at the cooling rate of  $0.4^{\circ}\text{C}$  min<sup>-1</sup>. Images of the tubes are recorded every six seconds using a

Monochrome camera, during which temperature was changed by 0.04°C. For each filter sample extract, two sets of freezing experiments were carried out. In the first set of experiments, sample extracts were untreated (no heating) for total IN concentration measurements. In the second set, the samples were heated to 95°C for 10 min to denature the IN activity of biological IN following Christner et al. (2008) and Garcia et al. (2012). The concentrations of active biological IN were calculated as the difference between the concentrations of active IN measured with and without heating. However, it should be noted that heat treatment may not inactivate every ice nuclei site of biological material and hence the values presented should be considered as the lowest possible estimates of biological IN.

Previous findings based on heat treatment (e.g., Garcia et al. 2012; Joly et al. 2014) showed that the relative contribution of biological IN decreases with temperature, with 97%–100% of total IN active at  $-8^{\circ}$ C and 77% at  $-12^{\circ}$ C as other particles including dust, become active at colder temperatures. Hill et al. (2014) showed that heat treatment (at 95°C) of bacterial samples obtained by leaf washing reduced the ice nucleation activity by >75% at  $-10^{\circ}$ C. According to Conen et al. (2011), heating to  $100^{\circ}$ C reduced IN activity at  $-12^{\circ}$ C by 70%–98%. O'Sullivan et al. (2015) showed that heat treatment (90°C) of soil samples containing organic decomposing matter reduced ice nucleation activity at  $-12^{\circ}$ C to  $\sim 1/10$ .

In addition, the concentration of active biological IN at temperatures colder than -15°C was estimated for the sample extract of 0911 [section 2e(2)] based on heating tests (95°C for 10 min) in FRIDGE-IMM. The methodology of drop freezing experiment is already described in section 2e(2).

# f. Classification of PBAPs based on SEM images

We innovated our own system of PBAP classification based on specimen SEM images collected from the available literature and created a list of distinct morphological features. These criteria are listed in Table 3 for the general size and morphological characteristics of different PBAP groups, based on the literature available. These characteristics form the basis for classifying PBAPs SEM images into basic groups.

After collecting the bioaerosol images, we classified them into common PBAP groups based on size and morphology by those criteria. Typical images of the bioaerosols collected from each group during this study are shown in Fig. 2. Fungal spores and associated fragments (group 1) were one of the most common classes of bioaerosols observed during our campaign. Fungi can grow in almost every ecosystem and are efficient in aerosolization (Adhikari et al. 2009; Löbs et al. 2020). The morphological characteristics of fungal spores have been well documented in global air and are summarized in Table 3 (Després et al. 2012, and references therein; Shi et al. 2003; Tamer Vestlund et al. 2014; Valsan et al. 2015, 2016; Priyamvada et al. 2017; Wu et al. 2019; Li et al. 2020). They appear in various forms, including globular, subglobular, elliptical, and elongated. Many of the spores possess the attachment scar and appear either with smooth or ornamented surfaces. The size range of particles from SEM images considered for

TABLE 3. Typical size ranges, concentrations in air, and general morphological characteristics of different PBAPs, based on available literature are given. Based on this information, PBAPs have been classified into different groups. Also enlisted are various studies referred to for classification of PBAPs.

PBAP type	Typical size $(\mu m)$ and number concentration $(m^{-3} \text{ of air})$	General morphological features	References
Fungal spores	Size: 1–50; most frequently 2–10 Concentration: 10 <sup>4</sup>	(i) Shape: Globose, elliptical, fusiform, asymmetric, lemon- shaped, barrel-shaped, curved; (ii) wall characteristics: Smooth, granular, reticulate, spines, warts; (iii) attachment scars, attachment pegs; (iv) other features: branched hyphae	Després et al. (2012, and references therein), Priyamvada et al. (2017), Li et al. (2020), Huffman et al. (2012), Barbosa (2018), China et al. (2016)
Bacteria	Size: 0.5–4 Concentration: 10 <sup>4</sup> (over land), 10–1000 (over ocean)	<ul><li>(i) Shape: Spherical, rodlike, helical;</li><li>(ii) wall: flagella, pili, capsules; (iii) arrangement: pairs, tetrads, clusters, chains</li></ul>	Després et al. (2012, and references therein), Li et al. (2020)
Pollen	Size: 10–50 Concentration: 10–1000	(i) Shape: Ellipsoid, fusiform, globose/spheroidal; (ii) presence of forrows; (iii) outer exine is usually sculptured; (iv) exine ornamentation like fossulate or microrugulate	Després et al. (2012, and references therein), Barbosa (2018, and references therein), Xu and de Craene (2013)
Plant/animal detritus	Size: Brochosomes—0.5; leaf litter—0.5–5 Concentration: —	Various shapes  (i) Shape: Football (brochosomes), spiral (epicuticular wax of plants), elongated (leaf litter)	Després et al. (2012, and references therein), Wittmaack (2005)
Algae	Size: 1–10 Concentration: 100	(i) Shape: Unicellular flagellates or amoeboids, colonial and nonmotile forms	Després et al. (2012, and references therein)

classification of PBAPs in this group is generally from 1 to  $20\,\mu m$ . The SEM images of fungal spores collected over Amazon rain forest (e.g., Huffman et al. 2012; Barbosa 2018; China et al. 2016) were referred while conducting the classification.

The images of bacteria (group 2) on Si wafer were clearer and were used for the size distribution. The basic morphological features of bacterial particles are spheres (coccus) and round-ended cylinders (bacillus). In addition, there may be few others with helically twisted shapes. Some bacterial cells grow separately while some rods or cocci grow in chains, grapelike clusters or form a cubic packet characteristically. The surface structures include flagella, pili, and capsules. A few representative images of bacillus and cocci shaped bacteria from the ATTO samples are shown in Fig. 2. We attempted to grow the bacteria from filter samples in agar solution, but no bacterial growth was observed. It should be noted that the filter samples were not immediately analyzed for bacterial growth and were stored in a freezer at  $-25^{\circ}$ C after sampling, which could have affected the viability of the bacteria.

Pollen grains (group 3) were broadly distinguished from fungal spores based on size and morphology. Typically, the size of pollen ranges from 10 to  $100\,\mu\text{m}$ . PBAPs are classified as pollen based on the general morphological characteristics of pollen grains given in Table 3. Barbosa (2018) provided an

extensive image database of pollen grains collected at the ATTO site and was frequently used for classification. From our SEM imaging, the size range of the pollen grains varied between 8 and  $20\,\mu\text{m}$ . Pollen grains with a diameter of 10 to  $30\,\mu\text{m}$  were frequently observed at the ATTO site, while larger pollen grains are generally absent high above the canopy except during some thunderstorm events (Barbosa 2018). Accordingly, our SEM analysis did not show a pollen grain presence greater than  $20\,\mu\text{m}$ . Observed pollen grains exhibited different shapes, including ellipsoid, fusiform, globose/spheroidal.

For any given are scanned area by SEM, about 2–4 brochosome clusters have been detected on the filter for each case and are assigned to group 4 (viral, plant/animal detritus). Each cluster consists of 3 to 40 brochosomes with an individual diameter of about 0.45  $\mu$ m. Brochosomes are intricately structured microscopic granules secreted by leafhoppers that are typically found on their body surface and more rarely, eggs (Wittmaack 2005). Group 4 was dominated by the presence of leaf litter followed by epicuticular wax of plants, insect scales, and other vegetation detritus. Viral particles were hardly detectable by our SEM analysis.

Somewhat surprisingly, during a rather large number of SEM investigations, no particle could be identified as algae

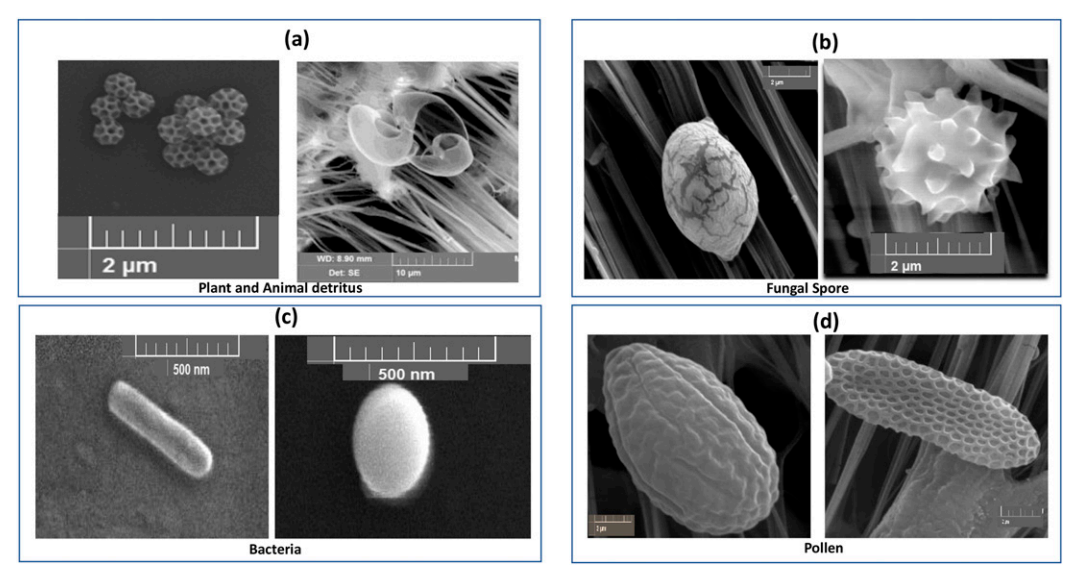


FIG. 2. Representative scanning electron microscopy images of (a) brochosomes and leaf litter (group: plant and animal detritus), (b) fungal spore, (c) bacteria, and (d) pollen from 0911N, 0912D, and 0913D. The scale is varying for each image and is shown separately.

(group 5; section 1), and therefore, algae are not shown in the size distribution presented here. A nearby water source close to the ATTO site had no measurable impact and nonzero concentrations of algal particles were never detected. However, algae can grow on leaves and soil. They could also be part of the long-range transport of marine particles from the Atlantic Ocean into the Amazon rain forest (Martin et al. 2010; Moran-Zuloaga et al. 2018). Backward trajectories (at 2 km) using the HYSPLIT model (see Fig. 1) suggest that a marine air mass from the Atlantic Ocean would have traveled over 5–6 days to reach the ATTO site. In summary, the absence of algae in our SEM analysis can be attributed to their low concentration in the air at the ATTO site and possible limitations in identifying them using SEM.

Moreover, it was a challenge to classify fragments of PBAPs seen in SEM images due to their irregular shape and lack of literature images available. Consideration was given to the external features of the background PBAPs on the filter paper that were easy to detach from the main PBAP particle. On this basis, fragments in the form of external spines, hyphae, etc. were then assigned to the corresponding broad group of the parent particle. In addition, visible characteristics of the wall and other aspects of each fragment were closely examined to identify its parent PBAP with matching features. Fragments smaller than  $1\,\mu m$  as well as fragments without such distinct discernible features could not be classified into main PBAP group. They are classified as "unidentified particles." Thus, the maximum uncertainties involved in the classification of fragments in the currents study are less than 5%.

#### 3. Results and discussion

a. The size distributions of PBAPs based on SEM analysis

Based on the SEM analysis of the filter and Si wafer samples, the size distributions for total primary bioaerosols as well as for various PBAP groups were constructed for 0911N, 0912D, and 0913D and are shown in Fig. 3. The size distribution of various PBAP groups based on SEM analysis of 5 and 1.2  $\mu$ m filter is provided in appendix C. In general, no difference in the size distribution of total PBAPs between day and nighttime samples is observed. The "coarse mode" (diameter: 1–10  $\mu$ m) bioaerosol particles were dominated by fungal spores as the corresponding size distribution shows a peak at 3–4  $\mu$ m. This is in agreement with the previous measurements by Huffman et al. (2012) and Whitehead et al. (2016), in which they attributed the peak in the coarse fluorescent biological size distribution to fungal spores.

Several types of fungal spores, such as *Basidiomycota*, *Cladosporium*, *Inocybe calospora*, and *Rhizopus*, were frequently observed in the ATTO samples. Most pollen grains observed during SEM were with  $D > 8 \, \mu \text{m}$ . "Fine mode" ( $D < 1 \, \mu \text{m}$ ) bioaerosol particles were dominated by the plant or animal detritus as well as bacteria. Overall, the total size distribution of PBAPs from the current study is in good agreement with previous observations by Huffman et al. (2012) and Whitehead et al. (2016) from a similar geographical location (see Fig. 3d).

The mean number concentrations of four PBAP groups, including fungi, bacteria, pollen, and viral, plant/animal detritus from SEM analysis are given in Table 4. Typically the number concentrations of fungal spores and pollens at the ATTO site were measured as  $\sim\!10^4$  and  $\sim\!10^3\,\mathrm{m}^{-3}$ , respectively, following typical concentrations in vegetated areas (Després et al. 2012, and references therein). Estimated mean number concentrations of bacterial particles are  $\sim\!10^5\,\mathrm{m}^{-3}$ , which is greater by one order of magnitude than those reported in the literature of typical bacterial concentrations of  $\sim\!10^4\,\mathrm{m}^{-3}$  in the air elsewhere (Després et al. 2012, and references therein).

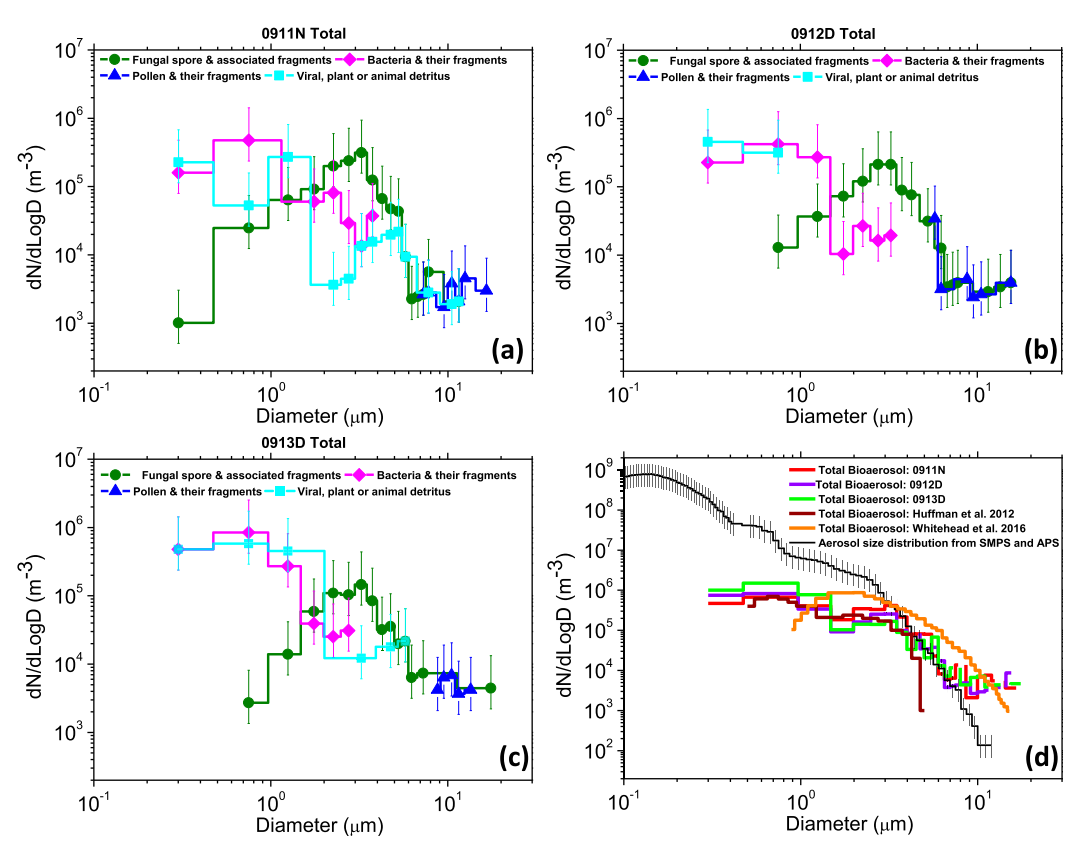


FIG. 3. The size distribution of PBAPs based on SEM analysis of samples (a) 0911N, (b) 0912D, and (c) 0913D. The size distribution of PBAPs shown here is from the combination of 5 and 1.2  $\mu$ m filters. (d) The total PBAP size distribution from each day is compared with the literature data. The total PBAP size distribution from our observations include unidentified PBAPs in addition to the other PBAP groups considered for classification. The combined aerosol size distribution from SMPS and APS on 14 Sep (thin black line) is also shown for reference.

A combined aerosol size distribution from the SMPS and APS on 14 September is shown in Fig. 3d to get an idea regarding the size distribution of total aerosol particles during the campaign. The SMPS and APS data were not available at the ATTO site for other sampling days considered here, as these instruments were not working on those days. Using aerosol size distributions (by SMSP + APS) on 14 September as a reference,  $\sim 11\%$  of coarse mode aerosol particles are of biological origin.

The total PBAP number concentration (with  $D>0.3\,\mu\mathrm{m}$ ) from SEM was compared with their independent estimations by FCM, as shown in Fig. 4. Overall, a good agreement is observed between SEM and FCM estimation of total PBAP

number concentration for samples from all three days discussed here. The number concentration of PBAPs from FCM was slightly lower than those from SEM since the abundance of PBAPs by FCM represents an approximately lower limit for the actual abundance of PBAPs. The concentrations of fluorescent biological aerosol particles (FBAPs) from the FCM analysis were  $3.3 \times 10^5$ ,  $1.06 \times 10^6$ , and  $1.19 \times 10^6$  m<sup>-3</sup> for 0911N, 0912D, and 0913D, respectively. These values are consistent with previously reported FBAP concentrations of about  $2 \times 10^5$  to  $1.2 \times 10^6$  m<sup>-3</sup> by Whitehead et al. (2016) in the central Amazon forest. Huffman et al. (2012) reported coarse mode FBAP concentration of about  $7.3 \times 10^4$  m<sup>-3</sup> over the Amazon rain forest. The lognormal size distribution was

TABLE 4. General size and mean number concentration of various PBAP groups based on our SEM analysis.

PBAP group	Typical size (μm)	Mean number concentration (m <sup>-3</sup> air) from SEM analysis
Fungal spores and associated fragments	1–10	$7.6 \times 10^4  (\pm 2.8 \times 10^4)$
Bacteria and their fragments	0.5–2	$4.2 \times 10^5 \ (\pm 1.98 \times 10^5)$
Pollen and their fragments	6–50	$1.07 \times 10^3  (\pm 673)$
Viral, plant/animal detritus	0.2–5	$4.1 \times 10^5 \ (\pm 1.8 \times 10^5)$

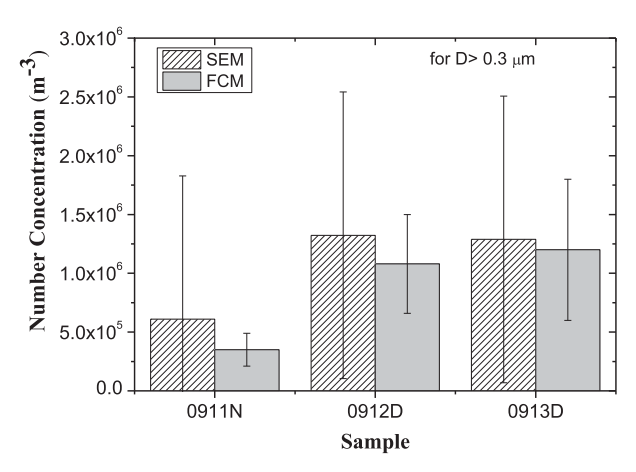


FIG. 4. Comparison of total bioaerosol particle number concentration ( $D>0.3\,\mu\mathrm{m}$ ) measured by scanning electron microscopy (SEM; left bars) with flow cytometry (FCM; right bars). Error bars for number concentrations measured by FCM were estimated based on independent runs of FCM for the same sample.

fitted to various PBAP groups based on our SEM analysis and resulting size distribution parameters are described in appendix B.

### b. Observations of total IN

The observations of total IN including deposition and condensation-freezing IN and immersion freezing IN are shown in Fig. 5. Figures 5a-c show the concentration of IN activated by deposition and condensation-freezing modes determined as a function of temperature and relative humidity over ice (RHice) obtained by the FRIDGE-STD measurements. No active IN at temperatures warmer than  $-20^{\circ}$ C was detected with this instrument, suggesting that their concentrations may have been lower than the detection threshold of  $0.01 L^{-1}$ . For a given temperature and RH<sub>ice</sub>, large day-to-day variability in IN concentration was observed. The results indicate that higher IN concentrations were associated with higher RHice at any given temperature. The mean IN concentration at -25°C ranged from 0.03 to 0.43 L<sup>-1</sup> for RH<sub>ice</sub> between 120% and 130%, in agreement with recent measurements by Schrod et al. (2020) at the ATTO site. During the field campaign, the highest concentration of deposition and condensation freezing IN measured by FRIDGE-STD was  $4.5 L^{-1}$  at  $-30^{\circ}$ C.

Figure 5d shows the cumulative number concentration of immersion freezing IN from separate experiments in LINDA and FRIDGE-IMM as a function of temperature. Overall, the concentration of immersion freezing IN was in the range of 0.0027– $40\,L^{-1}$  at a temperature between  $-6^\circ$  and  $-30^\circ$ C. The absence of any active IN in FRIDGE-IMM at a temperature  $>-15^\circ$ C could be associated with IN concentrations being below the detection threshold of  $0.15\,L^{-1}$ . The sample volume for LINDA samples was higher than the FRIDGE-IMM samples (Table 1); as a result, LINDA had a lower detection threshold of  $0.0014\,L^{-1}$ . The concentrations of IN from FRIDGE-STD at water saturation are lower than the

concentrations of immersion freezing IN from FRIDGE-IMM as FRIDGE-STD does not encapsulate the full extent of immersion freezing.

# c. Biological IN concentration from drop freezing experiments

The cumulative concentrations of biological and nonbiological IN determined by drop freezing arrays in LINDA are represented in Fig. 6 for 0911N, 0912D, and 0913D. The concentration of active biological IN between -5° and -15°C was determined by comparing measurements with and without heating. Freezing was observed with wide variance in onset temperature. Heating the sample extracts decreased the highest temperature of freezing, by 1°C in 0911N and 0913D to more than 4°C in 0912D. The active biological IN concentrations in air ranged from 0.0015 to  $0.047 L^{-1}$  between  $-6.5^{\circ}$ and -15°C and are in the range of previous biological IN measurements from rain samples (e.g., Xia et al. 2013; Pouzet et al. 2017). In general, the relative contribution of biological IN to the total IN decreased with decreasing temperature. The relative contribution of biological particles in the sample extracts of 0911N and 0912D ranged from ~100% of the total IN active at  $-8^{\circ}$ C to as low as  $\sim 86\%$  at  $-15^{\circ}$ C. In comparison, the contribution of biological particles to the total IN concentration in the sample extract of 0913D was much lower  $(\sim 62\% \text{ at } -13^{\circ}\text{C}).$ 

# 4. Empirical parameterization of heterogeneous ice nucleation for multiple groups of biological particles

- a. General equations for prediction of biological IN number concentration
  - 1) OVERVIEW OF EXISTING EMPIRICAL PARAMETERIZATION OF HETEROGENEOUS ICE NUCLEATION

The EP represented all known modes of heterogeneous ice nucleation (e.g., deposition and condensation/immersion-freezing modes) for multiple chemical species of aerosol and was proposed originally by Phillips et al. (2008, 2013). They assumed that for any scenario of aerosol chemistry, size, and loading, the number mixing ratio of active IN has contributions from several groups, including dust/metallic, black carbon, and organic aerosols. Thus, the number mixing ratio of active IN can be written as

$$n_{\rm IN} = \sum_{X} n_{{\rm IN},X},\tag{1}$$

where X = DM, BC, BIO, and solO for dust/metallic, black carbon, and primary biological and soluble organic aerosols, respectively.

The number concentration of IN activated by deposition and condensation/immersion-freezing modes from group X is proportional to the total aerosol surface area in that group:

$$n_{\text{IN},X} = \int_{\log[0.1\mu m]}^{\infty} \{1 - \exp[-\mu_X]\} \times \frac{dn_X}{d\log D_X} d\log D_X,$$
 (2)

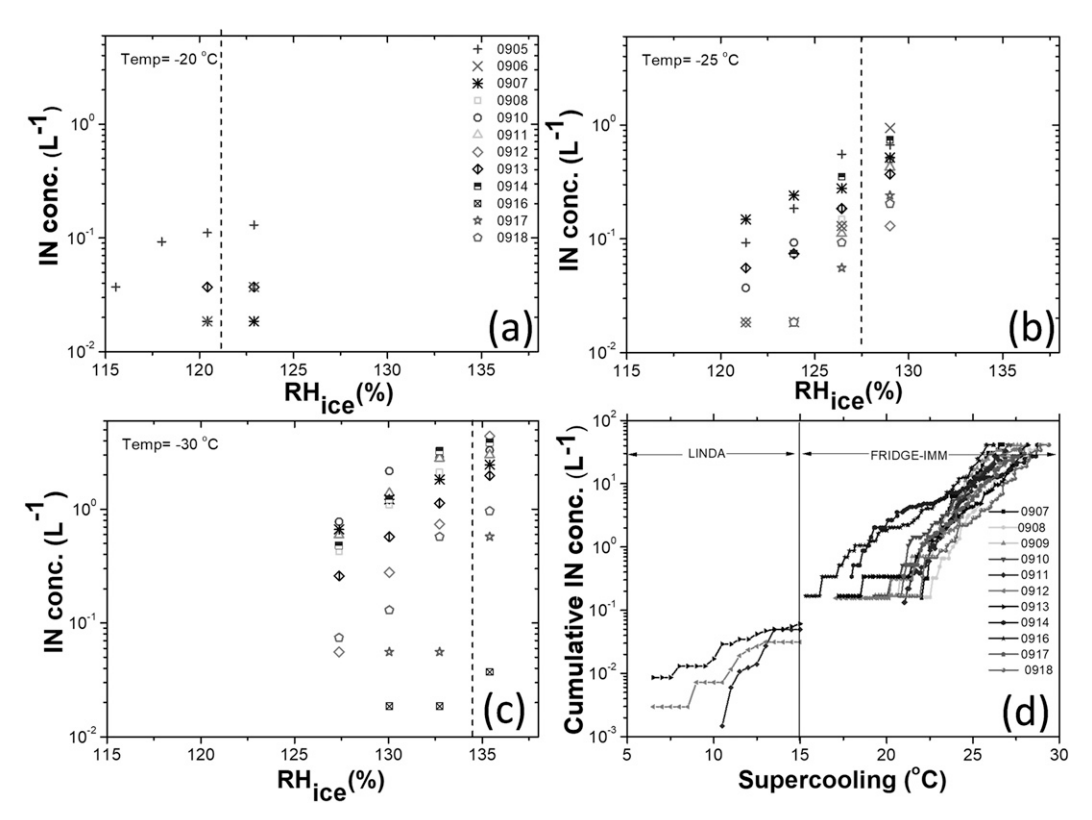


FIG. 5. The concentration of IN activated by deposition and condensation freezing mode in the FRIDGE-STD chamber at (a)  $-20^{\circ}$ , (b)  $-25^{\circ}$ , and (c)  $-30^{\circ}$ C. The dotted vertical lines in (a)–(c) indicate saturation with respect to water. (d) Cumulative IN concentrations activated by immersion freezing mode from separate experiments in FRIDGE-IMM are shown. The cumulative immersion freezing IN concentrations for 0911N, 0912D, and 0913D from the analysis in LINDA are also shown.

$$\begin{split} \mu_X &= H_X(S_i, \, T) \, \xi(T) \left( \frac{\alpha_X n_{\text{IN},1,*}}{\Omega_{X,1,*}} \right) \times \frac{d\Omega_X}{dn_X} \\ \text{for} \quad T &< 0^{\circ} \text{C} \quad \text{and} \quad 1 &< S_i < S_i^w \, . \end{split} \tag{3}$$

The  $\Omega_X$  is the total surface area of all aerosols with dry diameters larger than  $0.1 \, \mu \text{m}$ ,  $\mu_X$  is the average of the number of activated ice embryos per insoluble aerosol particle of size  $D_X$ . The number mixing ratio of aerosols in group X is given by  $n_X$ . A simplified version of Eqs. (2) and (3) is used for X = solO. The term  $H_X(S_i, T)$  is the empirically determined fraction  $(0 \le H_X \le 1)$  representing scarcity of nucleation under substantially subsaturated conditions. Also,  $\alpha_X$  is a fractional contribution from aerosol group X to the IN concentration. The empirical formulation presented in the current study only considers ice nucleation activity of biological particles with diameter larger than 0.1  $\mu$ m. However, a few biological particles and their fragments, macromolecules smaller than  $0.1 \mu m$  may act as IN and are not considered in the formulation presented here.

The number of ice crystals generated in a time step  $\Delta t$  is given by

$$\Delta n_i = \sum_X \max(n_{\text{IN},X} - n_{X,a}, 0) \equiv \sum_X \Delta n_{X,a},$$
 (4)

where  $n_{X,a}$  is the number mixing ratio of IN from group X that have already been activated. Additional details about the scheme and associated terms can be found in Phillips et al. (2008, 2013).

# 2) MODIFICATION OF SCHEME TO RESOLVE MULTIPLE GROUPS OF BIOLOGICAL IN

The original EP treated biological ice nucleation with only one species of IN. That assumption is changed as follows.

Here we now replace the previous X = BIO by five PBAP groups 1–5 (section 1) including fungal spores and associated fragments (FNG), pollen and their fragments (PLN), bacteria and their fragments (BCT), viral, plant/animal detritus (DTS), and algae (ALG). According to the EP for atmospheric ice nucleation by Phillips et al. (2008), the concentration of active IN from the given group within the given size interval  $d\log D_X$  depends on surface areas of given aerosol species. The empirical formulation mentioned below was not applied to algal particles since their size distribution from SEM measurements was not available. We used literature values of their frozen fraction to measure their ice nuclei activity and will be discussed in the latter part of this section.

For X = FNG, PLN, BCT, and DTS,

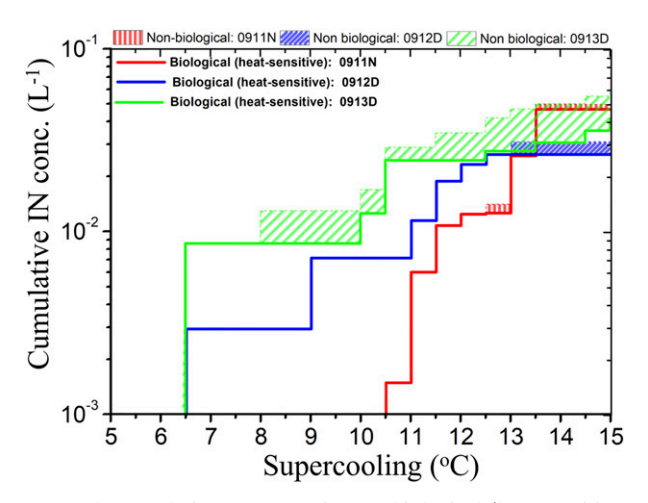


FIG. 6. Cumulative concentrations of biological (heat sensitive, thick lines) and nonbiological (heat resistance, shaded area) IN. The sum of two categories corresponds to the concentrations of total IN. The lower bound was considered for values below the detection limit. The IN concentrations showed here are from 5 and  $1.2\,\mu\mathrm{m}$  filters processed in LINDA.

$$\begin{split} n_{\text{IN\_BIO},X} &= \int_{\log[0.1\mu m]}^{\infty} \{1 - \exp[-\mu_X]\} \times \frac{dn_X}{d\log D_X} d\log D_X, \quad (5) \\ \mu_X &= H_X(S_i, T) \, \xi(T) \times \min\{[\exp(-\gamma_X T) - 1], \, 40\} \\ &\times \frac{1}{\omega_{X+*}} \frac{d\Omega_X}{dn_X} \quad \text{for} \quad T < 0^{\circ}\text{C}. \end{split} \tag{6}$$

Here,  $n_{\mathrm{IN\_BIO},X}$  is the number mixing ratio of IN active at temperature T in the Xth bioaerosol species;  $\Omega_X$  is the total surface area mixing ratio of particles with diameters  $D_X$  greater than  $0.1~\mu\mathrm{m}$  in group X and is a prognostic variable of the atmospheric model;  $d\Omega_X/dn_X \approx \pi D_X^2$ ;  $dn_X/d\log D_X$  is the normalized size distribution of given bioaerosol species X.

Particles with a diameter smaller than about  $0.2 \,\mu m$  that were not detected by the SEM analysis, but their absence merely reflects technical limitations of the setup. This is expected to have an insignificant effect on our empirical

formulation as the contribution of these smaller particles to the overall surface area mixing ratio is negligible. In the empirical formulation provided here, the surface area of a particle is more important than its mass. For 0911N, the relative contribution of particles in the size bin 0.1– $0.2~\mu m$  to the total surface area mixing ratio is only about 0.15% if the number concentration of particles in this size bin is assumed similar to that in the neighboring size bin with a larger diameter. Shape factors should also be considered when estimating the surface area of PBAPs. However, due to the complexity of the observed shapes of PBAPs we assumed spherical shape for all PBAPs and refrained from considering the shape factor in the estimation of surface area.

The factor  $\mu_X$  is the average number of potentially activated ice embryos per aerosol particle with diameter  $D_X$ . For lower freezing fractions  $\mu_X \ll 1$ , Eq. (5) can be written as  $n_{\text{IN BIO},X} = H_X(S_i, T)\xi(T)[\exp(-\gamma_X T) - 1] \times \Omega_X/\omega_{X,1,*}$ showing surface area dependence of predicted IN number concentrations. Also  $\omega_{X,1*}$  is an unknown parameter and depends on bioaerosol type with the dimensions of area (m<sup>2</sup>). In Eq. (6),  $H_X(S_i, T)$  is the empirically determined fraction (0  $\leq H_X \leq$  1) representing suppression of nucleation under substantially water-subsaturated conditions.  $H_X$ is expressed as a function of  $S_i$  and T by Phillips et al. (2008) with  $H_X = 1$  at water saturation. The slope of the fitted curve predicting activated IN is given by  $\gamma_X$ . The factor  $\xi$  considers the fact that drops are not observed to freeze at temperatures warmer than a threshold in the laboratory observations. Phillips et al. (2008) proposed  $\xi = \delta_1^0(T, T_1, T_2)$ , where  $\xi$  is 1 for  $T < T_1$  and 0 for  $T > T_2$  with cubic interpolation between and assumed  $T_1$  (-5°C) and  $T_2$  (-2°C) for all aerosol species.

For temperatures colder than  $-20^{\circ}$ C, lower slope values (45% of original) of the fit were prescribed based on observations of biological IN of 0911N at temperature between  $-20^{\circ}$  and  $-27^{\circ}$ C (see Fig. 9). The modified version of proposed parameterization [Eqs. (5) and (6)] for any  $T < 0^{\circ}$ C can be written as

$$n_{\text{IN\_BIO},X} = \int_{\log[0.1\mu m]}^{\infty} \{1 - \exp[-\mu_X]\} \times \frac{dn_X}{d \log D_X} d \log D_X,$$
 (7)

$$\mu_{X} = \begin{cases} H_{X}(S_{i}, T) \, \xi(T) \times \min\{[\exp(-\gamma_{X}T) - 1], \, 40\} \times \frac{1}{\omega_{X,1,*}} \frac{d\Omega_{X}}{dn_{X}}, & \text{for} \quad T > -20^{\circ}\text{C} \\ H_{X}(S_{i}, T) \, \xi(T) \times \min\{[\exp(-\gamma_{X}T) - 1], \, 40\} \times \exp[0.45 \times (T + 20)] \times \frac{1}{\omega_{X,1,*}} \frac{d\Omega_{X}}{dn_{X}}, & \text{otherwise.} \end{cases}$$

$$(8)$$

Equations (7) and (8) are applied for biological species, X = FNG, PLN, BCT, and DTS (groups 1–4, section 1). All variables used in the formulation are described in appendix A.

Regarding algal particles (group 5; section 1), a separate representation is proposed as follows. Since the concentrations

of algal particles at the ATTO site were much lower than our detection threshold ( $\sim 0.5 \, \mathrm{m}^{-3}$ ), we could not use a similar empirical treatment for them which was used for other PBAP groups. Generally, in atmospheric models, there may be situations where algae are more prolific and can influence the ice initiation. In such a scenario, their contribution to the total

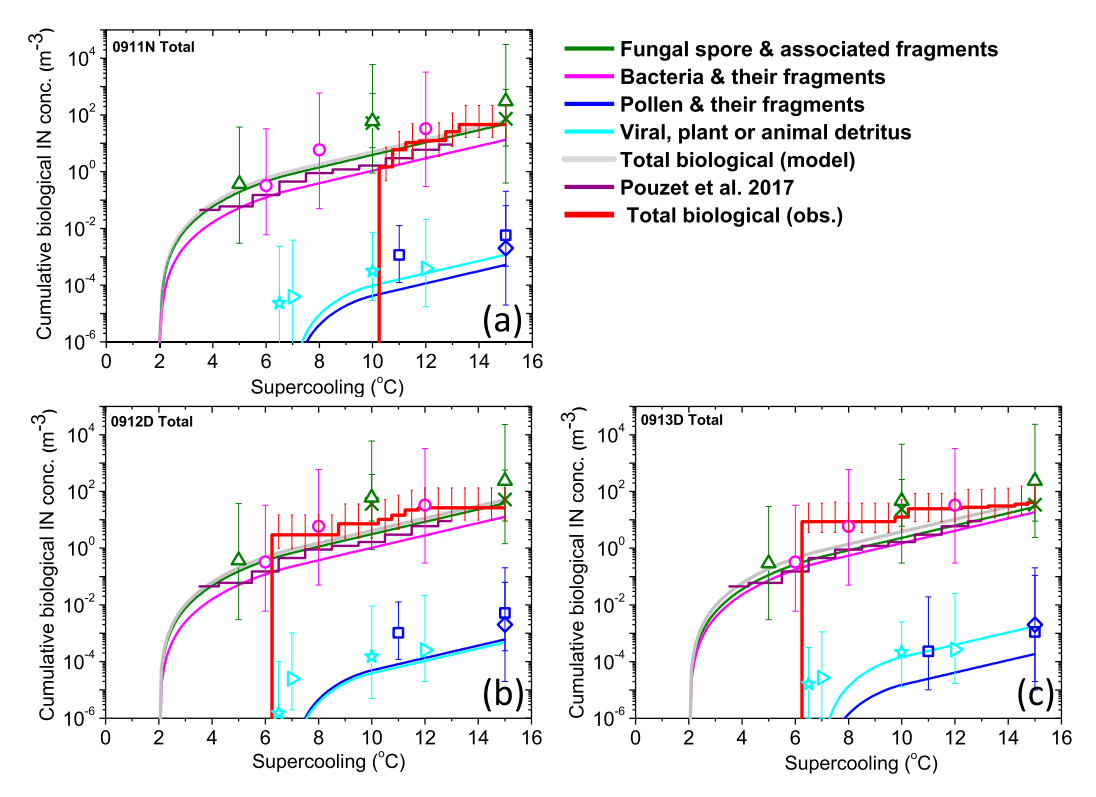


FIG. 7. Prediction of biological ice nuclei concentrations by new empirical parameterization based on the size distribution of PBAPs, shown as a function of temperature for various bioaerosol species. The total biological ice nuclei concentrations from the empirical parameterization (thick gray line) are compared with the observed values (thick red) from the drop freezing experiments with LINDA and with previous observations by Pouzet et al. (2017) (thick purple line). The prediction is based on the total size distribution ( $5 \mu m + 1.2 \mu m$ ) for each sampling day shown here. In addition, predicted values of biological IN are compared to previous observations listed in Table 6. Biological ice nuclei concentration of fungi based on active fractions measured by Haga et al. (2014) (green crosses) and O'Sullivan et al. (2015) (green triangles) are shown for comparison. The number concentrations of pollen as biological ice nuclei are shown based on Murray et al. (2012) (blue diamonds) and O'Sullivan et al. (2015) (blue squares). The bacterial ice nuclei concentrations based on Joly et al. (2014) (magenta circles). The leaf litter as ice nuclei are also shown based on Schnell and Tan-Schnell (1982) and Schnell and Vali (1976). Black dotted lines in the plot of 1.2  $\mu$ m filter represent the upper and lower bounds in predicting ice nuclei concentrations due to uncertainties in collection efficiency.

biological IN cannot be excluded. We, therefore, used the estimation of the frozen fraction for the algal particles (diatom cell, T. pseudonana) available in the literature (Wilson et al. 2015) to estimate the algal IN in the atmosphere. The relationship between the frozen fraction ( $f_{algae}$ ) of algae and temperature was established by inspection of extended data from Wilson et al. (2015, their Fig. 6):

$$f_{\text{algae}}(T) = A_1 + \frac{(A_2 - A_1)}{1 + 10^{(B+T) \times p}},$$
 (9)

where  $A_1 = -0.03$ ,  $A_2 = 0.993$ ,  $B = 27.73^{\circ}\text{C}$ , and p = 0.399. Also  $f_{\text{algae}}(T) = 0$  at  $T > -24^{\circ}\text{C}$  and  $f_{\text{algae}}(T) = 1$  at  $T < -35^{\circ}\text{C}$ . If the concentration of algal particles  $(n_{\text{algae}})$  in the air is known, then for X = ALG,

$$n_{\text{IN BIO},X} = f_{\text{algae}} \times n_{\text{algae}}.$$
 (10)

Algal IN estimates by Wilson et al. (2015) are based on samples collected from oceanic (Arctic, Atlantic, North Pacific) and coastal locations (British Columbia, Canada). Our scheme treats algal particles over the ocean but does not necessarily apply to the prediction of biogenic organic macromolecules which can act as efficient IN. Although they are biological in origin, these organic macromolecules are not classified as PBAPs as they are dissolved organic matter and therefore not primary (Knopf et al. 2018; Pummer et al. 2012, 2015; McCluskey et al. 2018). Such ice nucleating macromolecules are located on the surfaces of leaves, wood, and bark and can be washed down by rainwater (Felgitsch et al. 2018).

## b. Empirical determination of values of parameters

Based on above measurements of IN (Fig. 7 and appendix D) and size distributions (Fig. 3 and appendix C) for nine cases

TABLE 5. Details about most empirical parameters mentioned in sections 4a and 4b, together with their values, are given. The source of each fitting parameter is mentioned in parenthesis. The slope values are based on visual fit to observed data and are not derived from the variational analysis.

Symbol	Value	Source
γ <sub>FNG</sub> , γ <sub>PLN</sub> ,γ <sub>BCT</sub> , γ <sub>DTS</sub>	0.5°C <sup>-1</sup>	ATTO data (visual fit by eye)
$\omega_{\mathrm{FNG},1,*}$	$9.817 \times 10^{-5} \mathrm{m}^2$	ATTO data
ω <sub>PLN,1,*</sub>	$0.1 \text{ m}^2$	Constrained based on O'Sullivan et al. (2015)
$\omega_{\mathrm{BCT}.1.*}$	$9.12 \times 10^{-5} \mathrm{m}^2$	ATTO data
ω <sub>DTS.1.*</sub>	$0.1  \text{m}^2$	Constrained based on Schnell and Tan-Schnell (1982)
$T_{\rm FNG,1}, T_{\rm FNG,2}$	−7°, −2°C	Partly ATTO data (fit by eye); partly based on Richard et al. (1996), Després et al. (2012), and Kunert et al. (2019)
$T_{\mathrm{PLN},1},T_{\mathrm{PLN},2}$	−10°, −7°C	Prescribed based on Després et al. (2012) and Kanji et al. (2017, and references therein)
$T_{BCT,1}, T_{BCT,2}$	−7°, −2°C	Partly ATTO data (fit by eye); partly based on Després et al. (2012, and references therein)
$T_{\mathrm{DTS,1}},T_{\mathrm{DTS,2}}$	−10°, −7°C	Prescribed based on Schnell and Tan-Schnell (1982) and Després et al. (2012)

(section 2c), the values of active biological IN from groups 1–4 were estimated using proposed EP [Eqs. (5)–(8)]. The scope of the experimental derivation of estimates of all unknown parameters for each PBAP category was limited by several technical aspects of PBAP collection and processing for ice nucleation. A key problem we faced when observing samples was that the size distributions of various PBAP groups overlapped greatly. Consequently, it was not possible to isolate each PBAP group on any single filter. In addition, two of the four PBAP groups, including pollen and leaf litter, naturally have lower IN activity compared to fungi and bacteria (Després et al. 2012, and references therein). We aimed to overcome these difficulties by collecting our samples on different days under contrasting conditions in conjunction with inverse modeling, in the expectation that filters of contrasting porosities would be enriched differently in PBAP groups for the same airmass. However, there was a limit to the number of parameters that could be constrained by inverse modeling.

The relative abundance of the four groups of PBAPs and IN concentrations was seen to vary among the nine contrasting cases (Figs. 3, 7, C1, and D1). For agreement between observed and parameterized values, least squares fitting was used to estimate the universal law applicable to all nine cases so as to resolve the optimal values of the unknown parameters for PBAP groups 1-4, (Table 5). The concentration of total active biological IN from the EP was then compared to the observed biological IN concentrations for each of the nine cases (see Figs. 7 and D1). This variational analysis was performed by minimizing the weighted sum (E) over all nine cases of the mean squared error per case. The analysis was carried out with logarithm (base 10) of the active IN concentration for all temperatures where it is observed to be nonzero. Given the uncertainties associated with the size distribution of PBAPs on the 1.2 and 5  $\mu$ m and total filters (total of both), higher weights were applied for  $5 \mu m$  and total filters (100%) than for the 1.2  $\mu m$  filter (0.1%). Overall, the error of the optimal fitted prediction is about  $\pm 1 \,\mathrm{m}^{-3}$  of active IN per case.

The optimum values of the parameters inferred for the empirical scheme are shown in Table 5. The basis and sources of these fitting parameters are mentioned separately in this table. Based on the relationship between total measured biological IN concentrations at the ATTO site and freezing temperature, the value of slope parameter,  $\gamma$ , at  $T > -20^{\circ}\text{C}$  is prescribed as  $0.5^{\circ}\text{C}^{-1}$  and is assumed to be identical among PBAP groups 1–4 (section 1). The slope values are based on a visual fit to the observed IN data and may not be accurate for all PBAP groups. This value of the slope parameters fitted to our observation is in agreement with previous observations made by Vali [1994, Eq. (8) therein] and Pouzet et al. (2017) (Fig. 7).

The values of  $\omega_{X,1,*}$  for pollen and viral, plant/animal detritus were not prescribed directly from the literature. In the variational analysis, the values of the unknown parameter  $\omega_{X,1,*}$  of comparatively less active PBAP groups including pollen and viral, plant/animal detritus were constrained between 0.1 to 0.01 m² so that their estimated IN activity match the laboratory observation reported in the literature. Previous observations of leaf litter (a major part of group 4) from the tropics by Schnell and Tan-Schnell (1982) were used to constrain the values of  $\omega_{X,1,*}$  for group 4. For pollen, the  $\omega_{X,1,*}$  was constrained based on laboratory observations on active sites per gram of pollen mass (Betula pendula) by O'Sullivan et al. (2015). Additional details about these measurements used in the construction of the EP are given in Table 6.

In the current study, the values of  $T_1$  and  $T_2$  for determining the factor  $\xi$  are assumed to be variable for each bioaerosol type and are estimated based on the literature of previous observations or laboratory measurements. Therefore, the values of  $T_1$  and  $T_2$  for each PBAP group are denoted by  $T_{X,1}$  and  $T_{X,2}$ . Several studies have documented the activation of pollen at temperatures colder than  $-10^{\circ}$ C (Després et al. 2012; Kanji et al. 2017, and references therein). Freezing tests on leaf litter showed its activation at temperatures  $\sim -7^{\circ}$ C (Schnell and Tan-Schnell 1982; Després et al. 2012). Based on these observations,  $T_1$  was

TABLE 6. Origin of estimations of various biological IN concentrations (conc.) shown in Fig. 7. The mass of bioaerosol particles was calculated assuming aerosol particles to be spherical with a density of 1000 kg m<sup>-3</sup>. Observation of IN activity of pollen and leaf litter used in the construction of the scheme are mentioned in parentheses.

Species	Reference	Observed mass (kg m $^{-3}$ ) or number conc. (m $^{-3}$ )	IN conc. $(m^{-3})$
Fungi	1) O'Sullivan et al. (2015): Nucleation sites at $-5^{\circ}$ , $-10^{\circ}$ , and $-15^{\circ}$ C are $2.5 \times$	Mass: $1.51 \times 10^{-9}$ (0911N)	For 0911N: 0.38 (-5°C), 60.63 (-10°C), 303.16 (-15°C)
	$10^5$ , $4 \times 10^7$ , and $2 \times 10^8$ g <sup>-1</sup> , respectively	$1.52 \times 10^{-9} $ (0912D)	For 0912D: 0.37 (-5°C), 60.5 (-10°C), 302.53 (-15°C)
		$1.17 \times 10^{-9} $ (0913D)	For 0913D: 0.29 (-5°C), 46.8 (-10°C), 234.4 (-15°C)
	2) Haga et al. (2014): Active IN per fungi at $-10^\circ$ and $-15^\circ$ C are $5\times10^{-4}$ and $7\times10^{-4}$ , respectively	Conc.: $1.01 \times 10^5$ (0911N) $0.73 \times 10^5$ (0912D) $0.49 \times 10^5$ (0913D)	For 0911N: 52.80 (-10°C), 73.93 (-15°C) For 0912N: 36.9 (-10°C), 51.70 (-15°C) For 0913N: 24.81 (-10°C), 34.74 (-15°C)
Pollen	1) O'Sullivan et al. (2015) (used in construction of scheme): Nucleation	, ,	For 0911N: $1.15 \times 10^{-3} (-10^{\circ}\text{C})$ , $5.76 \times 10^{-3} (-15^{\circ}\text{C})$
	sites at $-10^{\circ}$ and $-15^{\circ}$ C are $2 \times 10^{3}$ and $10 \times 10^{3}$ g <sup>-1</sup> , respectively	$5.14 \times 10^{-10}  (0912D)$	For 0912D: $1.02 \times 10^{-3}$ (-10°C), $5.14 \times 10^{-3}$ (-15°C)
		$1.18 \times 10^{-10}  (0913D)$	For 0913D: $2.36 \times 10^{-4}$ (-10°C), $1.18 \times 10^{-3}$ (-15°C)
	2) Murray et al. (2012)		Pollen as potential IN is $2 \times 10^{-3}$ (-15°C)
Bacteria	1) Joly et al. (2014): Bacterial conc. was variable from $1.6 \times 10^3$ to $3.4 \times 10^4  \text{mL}^{-1}$ ; mean fraction of ice nucleation active bacteria at $-6^\circ$ , $-8^\circ$ , and $-12^\circ\text{C}$ are $0.01\%$ , $0.18\%$ , and $1.02\%$ , respectively; liquid water content was assumed $0.5  \text{g m}^{-3}$		0.32 (-6°C), 5.8 (-8°C), 32.5 (-10°C)
Leaf litter	1) Schnell and Tan-Schnell (1982):  Nucleus concentration at -6.5°C and -10°C is 60 and 800 g <sup>-1</sup> , respectively (used in construction of scheme)	Mass: $3.86 \times 10^{-10} $ (0911N)	For 0911N: $2.3 \times 10^{-5}$ ( $-6.5^{\circ}$ C), $3.08 \times 10^{-4}$ ( $-10^{\circ}$ C)
		$2.56 \times 10^{-11}  (0912D)$	For 0912D: $1.5 \times 10^{-6}$ (-6.5°C), $2 \times 10^{-5}$ (-10°C)
		$2.67 \times 10^{-10}  (0913D)$	For 0913D: $1.6 \times 10^{-5}$ (-6.5°C), $2.13 \times 10^{-4}$ (-10°C)
	2) Schnell and Vali (1976): Nucleus concentration at $-7^{\circ}$ and $-127^{\circ}$ C is 100 and $1000 \text{ g}^{-1}$ , respectively (for leaf litter in tropical climate zone)		For 0911N: $3.8 \times 10^{-5}$ (-7°C), $3.8 \times 10^{-4}$ (-12°C)
			For 0912D: $2.5 \times 10^{-5}$ (-7°C), $2.5 \times 10^{-4}$ (-12°C)
	,		For 0913D: $2.67 \times 10^{-5}$ (-7°C), $2.67 \times 10^{-4}$ (-12°C)
Total biological IN	Pouzet et al. (2017) (Fig. 1): Rainwater content was assumed 0.3 g m <sup>-3</sup> to convert concentrations to m <sup>-3</sup> of the air		0.06 (-5°C), 1.65 (-10°C), 6 (-12°C)

assumed to be  $-10^{\circ}$  to  $-7^{\circ}$ C for pollen and plant/animal detritus, respectively. Comparatively, fungi and bacteria are activated at temperatures warmer than  $-5^{\circ}$ C (Richard et al. 1996; Després et al. 2012; Kunert et al. 2019), and therefore,  $-7^{\circ}$  and  $-2^{\circ}$ C, respectively, were assumed for  $T_1$  of both.

Figure 7 and D1 shows the predicted number concentrations of crystals nucleated by various biological species based on size distributions from the total (5 and 2  $\mu$ m combined) and (see Fig. D1 for the 5 and 1.2  $\mu$ m filters). The predicted values of total biological IN by the EP are of similar magnitude in comparison with observations from the total (5  $\mu$ m + 2  $\mu$ m) and 5  $\mu$ m filters. The total number concentration was dominated by fungi and bacteria. Contributions to the measured IN

activity from pollen and detritus were lower by two orders of magnitude than those from fungi and bacteria at any given temperature.

Pollen grains can swell and explode from high humidityc exposure to emit numerous nanoscale particles, which are 10 to 1000 times smaller than intact particles. These smaller fragments may become aerosolized and act as efficient IN (O'Sullivan et al. 2015; Knopf et al. 2018). Given this, the contributions of pollen grains to total biological IN may be more important than suggested by our measurements.

Finally, the predicted total IN concentration is lower by one to two orders of magnitude when compared with the values obtained for the 1.2  $\mu$ m filters (Fig. 7; see also Fig. D1). This can be attributed to the uncertainties in estimating the

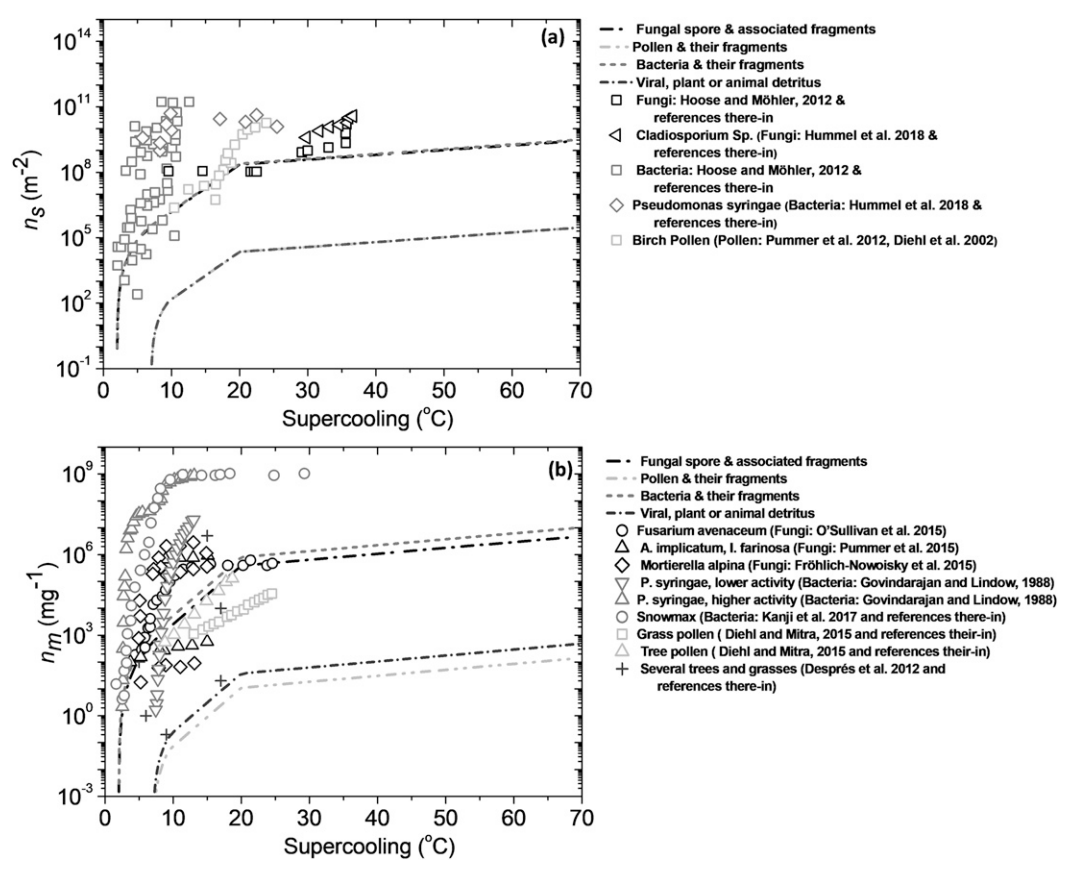


FIG. 8. (a) Ice-active surface site densities  $(n_s)$  and (b) ice-active mass site density for various PBAP groups from the proposed empirical parameterization (dotted lines) are shown as a function of temperature. The values for these two parameters from previous studies are also shown for a few biological species of PBAPs. Based on the literature, the values of  $n_s$  for fungi and bacteria (Hoose and Möhler 2012; Hummel et al. 2018) and pollen (Pummer et al. 2012; Diehl et al. 2002) are also provided for comparison. Similarly, literature-based estimations of  $n_m$  are also provided for fungi (O'Sullivan et al. 2015; Pummer et al. 2015; Fröhlich-Nowoisky et al. 2015), bacteria (Govindarajan and Lindow 1988; Kanji et al. 2017), pollen (Diehl and Mitra 2015), and leaf litter (Després et al. 2012).

collection efficiency of  $5 \mu m$  filters and hence to the size distributions of bioaerosol particles on  $1.2 \mu m$  filters.

# 5. Comparison of the empirical scheme with independent observations

The new EP is also compared with previous laboratory data and field observations, not used in its construction (as shown in Figs. 7 and D1). Additional details on the origin of these datasets and corresponding calculations are given in Table 6. The total concentration of PBAP IN predicted by EP is in good agreement with previous observations for rainwater samples from Opme (France) by Pouzet et al. (2017). For fungi, estimations of nucleation sites per gram of fungal mass (*Fusarium avenaceum*) (O'Sullivan et al. 2015) and active IN per fungus (*Basidiomycota* spores) (Haga et al. 2014) were used to calculate their contribution as IN for the observed mass and number concentration of fungi over the Amazon. According to previous studies by Murray et al. (2012, and references

therein), the number concentration of birch pollen as potential IN is typically  $2\times 10^{-3}\,\mathrm{m}^{-3}$  at  $-15^{\circ}\mathrm{C}$ . Based on ice nucleation activity of bacteria isolated from cloud water (Puy de Dôme, France) by Joly et al. (2014), number concentrations of potential INA bacteria were estimated  $\sim 0.32$  and  $5.8\,\mathrm{m}^{-3}$  of cloud air at temperatures  $-6^{\circ}$  and  $-8^{\circ}\mathrm{C}$ , respectively. The active IN concentration from leaf litter per m³ of air based on measurements by Schnell and Vali (1976) for leaf litter from tropical regions are also shown for comparison with parameterized values. When the uncertainty limits are considered, the EP's predicted PBAP IN concentrations are in agreement with available literature data.

Various metrics are used in the previous studies to represent ice nucleation abilities of various PBAP groups. The most commonly used metrics include 1) ice-active surface site densities  $(n_s)$ ; 2) ice-active mass site densities  $(n_m)$ , an analog to  $n_s$ , but mass equivalent; and 3) activated fraction (Kanji et al. 2017, and references therein). To represent our proposed EP [section 4a(2)] in terms of these common metrics, we estimated

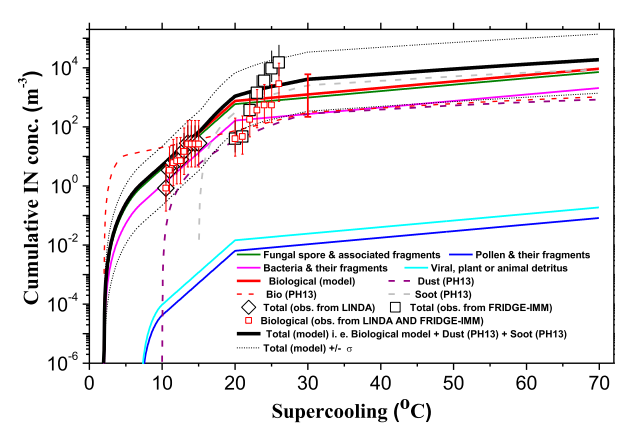


FIG. 9. The number concentration of biological ice nuclei predicted by empirical parameterization as a function of supercooling in a water-saturated air parcel. The number concentrations of dust, soot, and biological ice nuclei predicted by the empirical ice nucleation scheme by Phillips et al. (2013) (mentioned as PH13 in the plot) are also shown for comparison. The error bars of observed IN concentrations indicates the standard deviations estimated based on the uncertainties in the measurements. An error bar in thick red on the biological (model) line indicated uncertainties in the estimated biological IN at a temperature colder than  $-15^{\circ}$ C.

the mean values of  $n_s$  and  $n_m$  for various PBAP groups based on their IN activity, surface area mixing ratio, and mass in the nine cases considered in the study.

Figure 8 shows the dependence of these variables from the EP on temperature. The values of these two parameters for limited species of PBAP groups from the available literature are also shown for reference. However, there is a considerable spread in the literature data. At any given temperature, our estimated values of  $n_s$  and  $n_m$  for PLN and DTS by EP were much lower (by three orders of magnitude) when compared with our prediction of FNG and BCT as observed in the literature data (Kanji et al. 2017, and references therein). The values of  $n_m$  for group 4 (mostly leaf litter) are in good agreement with literature data. The literature values of  $n_s$  and  $n_m$  for snowmax and *Pseudomonas syringae* bacteria are much

higher than our estimated values (see Fig. 8). For any given PBAP group, the published observations of  $n_s$  and  $n_m$  show large variations among different biological species (Kanji et al. 2017, and references therein) which limits their direct comparison with our estimated values of the EP, which apply to entire groups of PBAPs. At a temperature of  $-10^{\circ}$ C, for example,  $n_m$  of three species of fungal spores showed a wide variation over four orders of magnitude.

# 6. Application of empirical parameterization in a parcel model for an idealized case

The new EP of biological ice nucleation is applied in an idealized 0D parcel model to shed light on some ramifications for natural ice initiation arising from the formulation. For simplicity, there are no microphysical processes included in the parcel model except for the heterogeneous ice nucleation. The adiabatic parcel starts at  $20^{\circ}$ C, rises to  $-50^{\circ}$ C and humidity is artificially prescribed corresponding to exact water saturation. Input size distributions of PBAPs (groups 1–4) to the empirical scheme are prescribed from observations for the case of 0911N. An EP from Phillips et al. (2013) was applied for nonbiological IN species including mineral dust/metallic and soot. The climatological values [from Model of Ozone and Related Chemical Tracers (MOZART)] of mass mixing ratios for dust  $(2.9 \times 10^{-10} \,\mathrm{kg \, kg^{-1}})$  and soot  $(3 \times 10^{-11} \,\mathrm{kg \, kg^{-1}})$ over the ATTO site were prescribed for estimating their contribution as IN. Total PBAP size distributions were prescribed based on observations on 0911N. For algae, quantitative measurements of their abundance in the ambient air are rare and so algal particles were not included in the simulation shown here.

Figure 9 shows the predicted number concentration of active biological IN from multiple species as well as the total IN. Compared with the original prediction by Phillips et al. (2013), the total biological IN predicted by the new empirical scheme differs up to one order of magnitude at T > -15°C and by about half an order of magnitude at T < -15°C. The original EP by Phillips et al. (2013) does not resolve individual groups of PBAPs. It was based on the ice nucleation of a bacterial

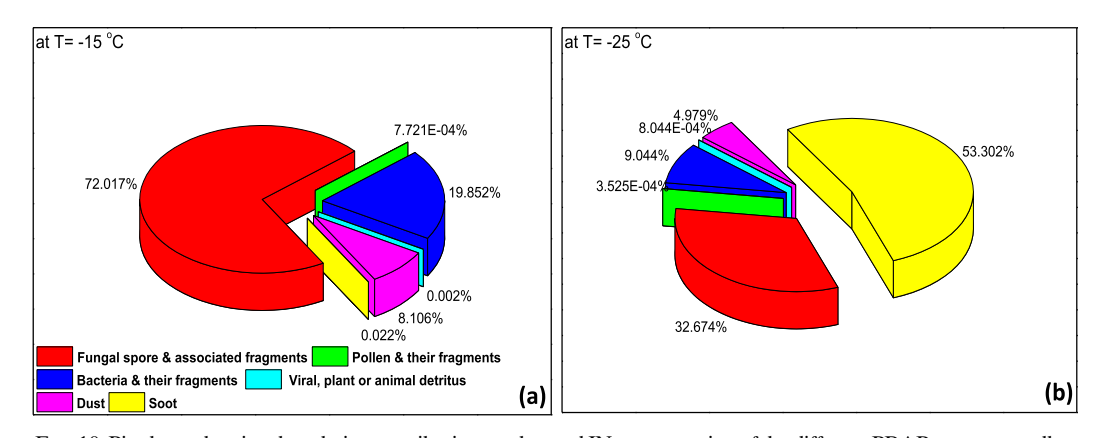


FIG. 10. Pie charts showing the relative contributions to the total IN concentration of the different PBAP groups as well as dust and soot particles at (a)  $T = -15^{\circ}$ C and (b)  $T = -25^{\circ}$ C for the parcel model simulation shown in Fig. 9.

strain observed in the laboratory that may not represent the large variations in ice nucleation characteristics observed among different PBAP groups.

Overall, total IN concentrations predicted by the model are in good agreement with the concentrations observed at the ATTO site (Fig. 9). Moreover, relative contributions to the total IN concentration of the different PBAP groups as well as dust and soot particles from this simulation are shown in Fig. 10. Biological particles dominate the predicted total IN concentrations at a temperature warmer than  $-20^{\circ}$ C and at colder levels dust, and soot particles became increasingly important in determining the total IN concentrations in the cloud.

#### 7. Conclusions

A modification to the flexible framework for treating multiple species of atmospheric IN in terms of empirical observations from the real atmosphere, namely, the "empirical parameterization" (EP), is proposed in the current study. This framework treats all known and empirically quantified modes of heterogeneous ice nucleation (e.g. deposition, condensation/immersion-freezing, inside-out and outside-in contact freezing). The previous single species for biological IN has been replaced by five major PBAP groups including FNG, PLN, BCT, DTS, and ALG. The new treatment has been fitted to observations of PBAPs in a field campaign at the ATTO site in the central Amazon. Some literature data are also used to constrain some aspects of this bio-EP. The new empirical treatment will allow atmospheric models to resolve the IN activity of these PBAP groups explicitly.

Amazonian PBAPs were collected on PTFE membrane filters and Si wafers for use in drop freezing experiments, ice nuclei activation in the cloud chamber, and SEM/EDX analysis. The EP was constructed from coincident observations of PBAP size, composition, concentration, and ice nucleating ability, and predicts numbers of active IN in each of the five groups of PBAPs.

The measured IN concentrations activated by deposition and condensation-freezing modes varied over three orders of magnitude throughout the campaign and strongly depended on the processing temperature and ice supersaturation in the chamber. At  $-25^{\circ}$ C, the measured IN concentrations activated by deposition and condensation-freezing mode ranged from 0.002 to  $1\,\mathrm{L}^{-1}$  for ice supersaturations of 21% and 28%, respectively. The filter samples were analyzed in LINDA to estimate biological IN active between  $-5^{\circ}$  and  $-15^{\circ}$ C. Filter and Si wafer samples were analyzed under SEM to measure the size distribution of common PBAP species. For each case, more than 300 images of bioaerosol particles were used.

The observed bioaerosols included brochosomes, fungal spores, bacteria, canopy debris (e.g., leaf and insect fragments, plant waxes), and less commonly pollen and insect scales. Overall, size distributions were observed to be bimodal and were like previous measurements from similar geographical locations (e.g., Huffman et al. 2012; Whitehead et al. 2016). The observed size distributions of PBAP groups have provided constraints primarily on their surface areas in determining

their ice nucleation activity. The size distribution of total bioaerosol particles was consistently dominated by a submicron peak associated with either viral, plant/animal detritus, or bacterial particles. The coarse mode of PBAPs observed in the current study was dominated by fungal spores consistent with previous observations (e.g., Huffman et al. 2012). The total number concentration of bioaerosols (with  $D>0.3\,\mu\mathrm{m}$ ) inferred by our SEM analysis is in good agreement with FCM analysis.

The total number concentration of biological IN predicted by the proposed parameterization scheme for the Amazon location was dominated by fungi and bacteria, with only a very minor role for pollen and detritus. For PBAP groups considered here, the active IN concentrations predicted by the scheme, and independent observational data not used in its construction, were consistent with the same order of magnitude. Implementation of the scheme in the 0D parcel model showed that biological IN account for most of the total ice nuclei activation at temperatures  $> -20^{\circ}\text{C}$ . At colder temperatures, dust and soot become more important to ice nucleation than biological IN, and increasingly so with more supercooling.

Thus, the new EP qualitatively reproduces the previous observations in the Amazon basin by Prenni et al. (2009) of biological IN determining the total IN concentrations at freezing temperatures warmer than -25°C. They showed that mineral dust became increasingly more important for ice nucleation at temperatures colder than -27°C. In their transmission electron microscopy, no soot IN were observed. However, it should be noted that their observations were limited to the wet season when there must have been little or no biomass burning. Biomass burning conditions are characteristics of the Amazon dry season and are maximum around September. Thus, soot particles resulting from biomass burning can play an important role in determining the ice nucleation at colder temperatures during the dry season, as suggested by our parcel model simulation. Recent observations by Schill et al. (2020) reported that black carbon from biomass burning contributes, at most, 10% to IN  $(-36^{\circ} \le$  $T \leq -11^{\circ}$ C). Nevertheless, the ability of black carbon emitted from biomass burning to act as IN is currently uncertain. Relative contributions of dust and soot to the ice nucleation shown in our parcel model simulations are limited to a case study and will be highly variable depending on the abundance of these aerosol species in the atmosphere.

To conclude, a modification of the EP is proposed based partly on Amazonian field observations, resolving the IN activity of the five basic groups of PBAP.

Acknowledgments. The work was funded by an award to Vaughan Phillips (VTJP) from the Swedish Research Council (Vetenskapsradet), related to the investigation of bioaerosol effects on clouds (Award Number: 2015-05104). VTJP directed the study. For the operation of the ATTO site, we acknowledge the support by the Max Planck Society, the German Federal Ministry of Education and Research (BMBF Contracts 01LB1001A, 01LK1602A, and 01LK1602B) and the Brazilian Ministério da Ciência, Tecnologia e Inovação (MCTI/FINEP

TABLE A1. Symbols used in this paper, along with their descriptions and units.

Notation	Description	Value and units
D	Diameter	m
$D_g$	Median diameter	m
$f_{ m algae}$	Frozen fraction of algal particles from Wilson et al. (2015)	_
$H_X$	Fraction reducing ice nuclei activity at low $S_i$ , warm $T$	_
max	Maximum value	_
min	Minimum value	_
N	Total aerosol number concentration	$\mathrm{m}^{-3}$
$n_s$	Ice-active surface site density	$\mathrm{m}^{-2}$
$n_m$	Ice-active mass site density	$kg^{-1}$
$n_X$	Number mixing ratio of particles in PBAP group X	$\mathrm{kg}^{-1}$
$n_{ m IN~BIO}$	Total number mixing ratio of active biological IN predicted	$kg^{-1}$
$n_{\text{IN\_BIO},X}$	Contribution to $n_{\text{IN BIO}}$ from PBAP group $X$	$kg^{-1}$
$n_{X,a}$	Number of aerosols in PBAP group $X$	$kg^{-1}$ $kg^{-1}$
$n_{X,a,\mathrm{cn}}$	Number mixing ratio of contact IN for group $X$	$kg^{-1}$
$n_{X,a,\mathrm{liq}}$	Number of interstitial IN in group X lost by becoming immersed	$kg^{-1}$
$n_{X,\mathrm{imm}}$	Number of IN from group X immersed in cloud liquid	$kg^{-1}$
$Q_r$	Mixing ratio of rain	$kg kg^{-1}$
$\widetilde{Q}_X$	Mixing ratio of aerosol in group $X$	$kg kg^{-1}$
RH <sub>ice</sub>	Relative humidity over ice	%
$S_i$	Saturation ratio of vapor with respect to ice	_
t	Time	S
T	Temperature	°C
$T_{X.1}$	Colder threshold temperature for onset of freezing for group $X$	°C
$T_{X,2}$	Warmer threshold temperature for onset of freezing for group $X$	°C
$v_t$	Fall speed of raindrop in given size bin	$\mathrm{m~s}^{-1}$
w	Vertical velocity of air	${ m m~s}^{-1}$
	Geometric standard deviation	
X = X	Label for four PBAP groups [fungal spores and associated fragments (FNG), pollen and	_
21	their fragments (PLN), bacteria and their fragments (BCT), viral, plant/animal detritus	
	(DTS), and algae (ALG)]	
$\xi(T)$	Fraction that is zero for $T > T_{X,2}$ (°C) and 1 for $T < T_{X,1}$ (°C), being $\delta_1^0(T, T_{X,1}, T_{X,2})$ for	$0 \le \xi \le 1$
5(1)	$T_{X,1} < T < T_{X,2}$ (°C) for $X = \text{FNG}$ , PLN, BCT, DTS	$0 = \zeta = 1$
$\Omega_X$	Total surface area of all bioaerosols $> 0.1 \mu m$ in diameter in group X	$m^2 kg^{-1}$ of air
$\Omega_{X   ext{int}}$	Interstitial component of $\Omega_X$	$m^2 kg^{-1}$ of air
$\Omega_{X,\mathrm{rain}}$	Total surface area of all aerosols with $D > 0.1 \mu\text{m}$ in group X inside raindrops	$m^2 kg^{-1}$ of air
$\delta_a^b(y, y_1, y_2)$	Cubic interpolation function equal to $a$ at $y \le y_1$ and to $b$ for $y \ge y_2$ , while $\delta_a^b = a_0 + a_1 y + a_2 y_2$	in kg of an
$O_a(y, y_1, y_2)$	case interpolation random equal to $u$ at $y = y_1$ and to $b$ for $y = y_2$ , while $a_a = u_0 + u_1 y + u_2 y^2 + u_3 y^3$ for $y_1 < y < y_2$ , where $a_0 = B$ , $a_1 = Ay_1y_2$ , $a_2 = -A(y_1 + y_2)/2$ ,	_
	and $a_3 = A/3$ with $A = 6(a - b)/(y_2 - y_1)^3$ and $B = a + Ay_1^3/6 - Ay_1^2y_2/2$ (adopted from	
	Phillips et al. 2008)	
	Average number of ice embryos per aerosol particle	
$\mu_X$	Slope value of the fit for $X = \text{FNG}$ , PLN, BCT, and DTS each of four PBAP group	$^{\circ}\mathrm{C}^{-1}$
$\gamma_X$		
$\alpha_X$	Fraction of $n_{\text{IN},1,*}$ from IN activity group $X = \{\text{DM}, \text{BC}, \text{O}, \text{solO}\}$	{2/3, 1/3–0.06, 0.06 m <sup>2</sup>
$\omega_{X,1,*}$	Baseline coefficient of PBAP for X = FNG, PLN, BCT, and DTS	
$\Delta t$	Model time step Difference in freezing temperature between contact and bulk water modes	s 4.5°C
$\Delta T_{\rm CIN}$	Difference in freezing temperature between contact and bulk water modes	4.3 C

Contract 01.11.01248.00) as well as the Amazon State University (UEA), FAPEAM, LBA/INPA and SDS/CEUC/RDS-Uatumã. This paper contains results of research conducted under the Technical/Scientific Cooperation Agreement between the National Institute for Amazonian Research, the State University of Amazonas, and the Max-Planck-Gesellschaft e.V.; the opinions expressed are the entire responsibility of the authors and not of the participating institutions. Further, we thank all people involved in the technical, logistical, and scientific support of the ATTO project. All aerosol samples collected at the ATTO site are property of the University of

São Paulo. Paul DeMott acknowledges support from the U.S. Department of Energy, Office of Science (BER), Atmospheric System Research (DE-SC0018929) and U.S. National Science Foundation Award 1660486. Daniel Knopf acknowledges support by the U.S. Department of Energy, Office of Science (BER), Atmospheric System Research (DE-SC0016370 and DE-SC0020006) and NASA Award NNX17AJ12G. Heinz G. Bingemer and Jann Schrod acknowledge funding by Deutsche Forschungsgemeinschaft (DFG) under the Research Unit FOR 1525 (INUIT) and from the European Union's Seventh Framework Programme (FP7/2007-2013) project BACCHUS

TABLE B1. Parameters of lognormal size distribution of various PBAP groups based on our SEM analysis. Here N is the total aerosol number concentration,  $D_g$  is the median diameter, and  $\sigma_g$  is geometric standard deviation. When implemented in a cloud model, the value of N is free to evolve during the simulation without the values below. For viral, plant/animal detritus, the ratio of numbers in both modes in the model always follows the ratio of N values below but with a total number in both modes that is free to evolve. For algae, we have used the size distribution parameters from literature (Després et al. 2012) with  $D_g = 5 \mu m$ ,  $\sigma_g = 1.5$ , and  $N = 0.5 \times 10^3 \, \text{m}^{-3}$ .

PBAP group	Parameters of lognormal size distribution	
Fungal spores and associated fragments	$D_g$	2.5 μm
	$\sigma_g^\circ$	1.8
	$\stackrel{\circ}{N}$	$7 \times 10^4  \mathrm{m}^{-3}$
Bacteria and their fragments	$D_g$	$0.7~\mu\mathrm{m}$
		1.7
	$rac{\sigma_g}{N}$	$4.5 \times 10^5 \mathrm{m}^{-3}$
Pollen and their fragments	$D_g$	9 μm
		1.5
	$\sigma_g \ N$	$1.1 \times 10^3 \mathrm{m}^{-3}$
Viral, plant/animal detritus	Fine mode with	
· •	$D_{g}$	$0.5  \mu \mathrm{m}$
	$\sigma_g^{\circ}$	1.4
	$\stackrel{\circ}{N}$	$3 \times 10^5  \mathrm{m}^{-3}$
	Coarse mode with	
	$D_{g}$	$3.6 \mu\mathrm{m}$
	$\sigma_g$	1.4
	$\stackrel{\circ}{N}$	$7 \times 10^{3}  \mathrm{m}^{-3}$

under Grant Agreement 603445. Susannah Burrows acknowledges support by the U.S. Department of Energy (BER), through the Early Career Research Program. The authors gratefully acknowledge the NOAA Air Resources Laboratory (ARL) for the provision of the HYSPLIT transport and dispersion model. SP and VJTP would like to thank Dr. Thara Prabhakaran for providing the filter holder. We are very grateful to Marcin Jackowicz Korczynski and Tomas Karlsson for providing the vacuum pump and other sampling tools. The authors wish to thank Tina Šantl-Temkiv, Sylvie Tesson, Jakob Löndahl, and Cybelli Barbosa for their help with SEM image analysis and valuable suggestions. We are grateful to Reiner Ditz, Andrew Crozier, and Stefan Wolff for their help with organizing logistics for a visit to the ATTO site. SP would like to thank Sonali Patade for her help in correcting grammar and language of the manuscript.

Data availability statement. The data that support the findings of this study are available from the corresponding author, Sachin Patade, on reasonable request. A copy of the EP scheme including the present addition is also available on request.

### APPENDIX A

### **List of Symbols**

Symbols used in the present paper are listed and described in Table A1.

### APPENDIX B

# **Parameters of Lognormal Size Distribution**

The following lognormal distribution function was fitted to observed size distributions of various PBAP groups at the ATTO site:

$$\frac{dN(D)}{d\log(D)} = \frac{N}{\sqrt{2\pi}\log\sigma_g} \exp\left\{\frac{-\left[\log(D/D_g)\right]^2}{2(\log\sigma_g)^2}\right\}, \quad (B1)$$

where N is the total aerosol number concentration, and  $D_g$  and  $\sigma_g$  are the parameters of a lognormal distribution:  $D_g$  is the median diameter, and  $\sigma_g$  is geometric standard deviation (polydispersity). These parameters for various PBAP groups are enlisted in Table B1.

#### APPENDIX C

### PBAP Size Distribution from 5 and 1.2 $\mu$ m Filter

The size distribution of various PBAP on 5 and 1.2  $\mu$ m filter is provided in Fig. C1.

#### APPENDIX D

# Model Prediction of Biological Particles for 5 and $1.2 \mu m$ Filters

Prediction of biological ice nuclei concentrations by new empirical parameterization based on the size distribution of PBAPs on 5 and 1.2  $\mu$ m filter is shown in Fig. D1.

### APPENDIX E

# Implementation of Empirical Parameterization in an Atmospheric Model

The present EP scheme slots into the EP framework for heterogeneous ice nucleation already described in Phillips et al. (2008, 2013). Their framework represents all modes of heterogeneous ice nucleation. The EP described in this study is

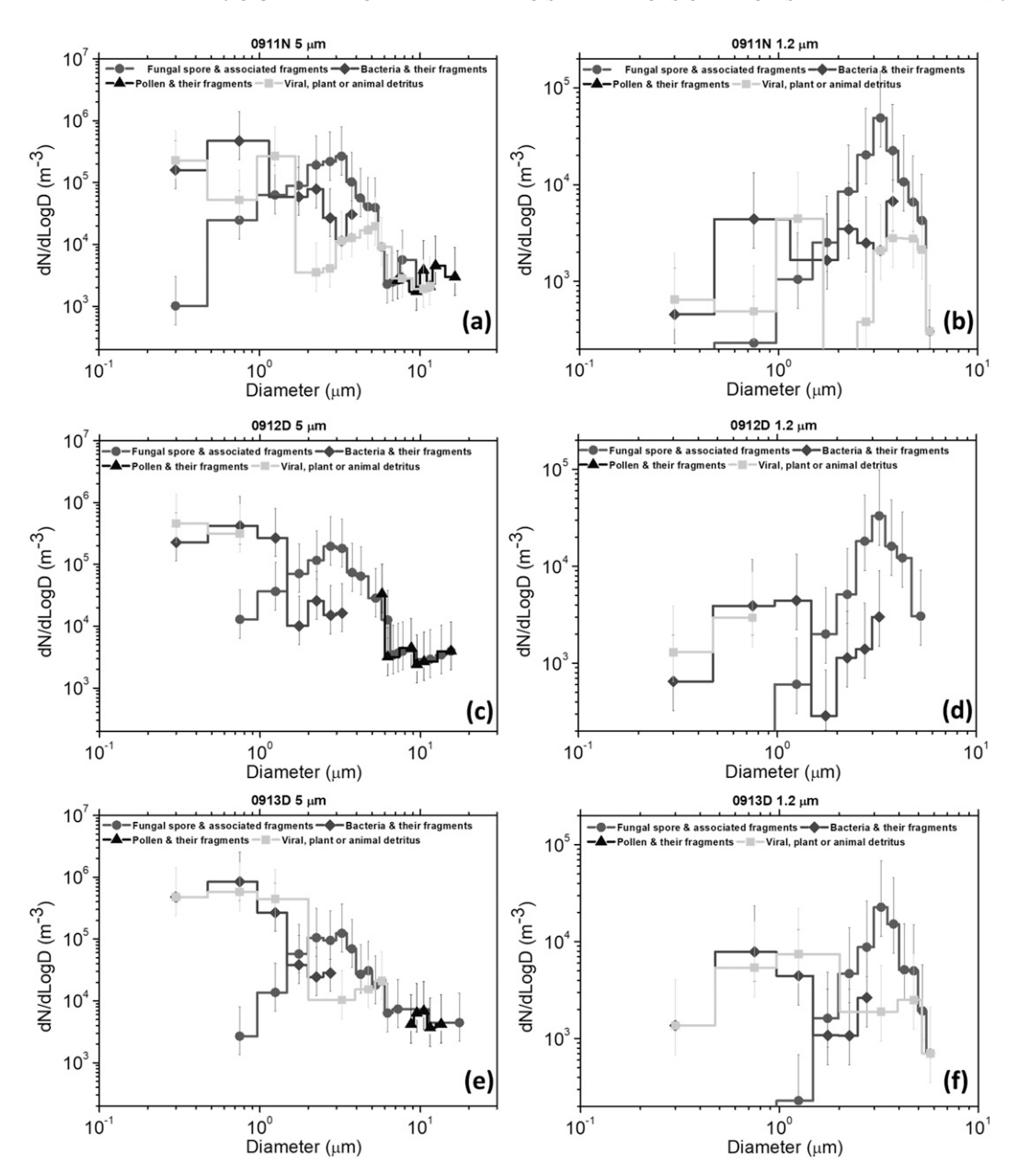


FIG. C1. The size distribution of PBAPs based on SEM analysis of 5 and 1.2  $\mu$ m filter.

for ice nucleation through deposition and condensation- and immersion-freezing mode.

To implement the scheme in a cloud model, each group X of IN is partitioned into prognostic components which are interstitial and immersed in cloud droplets to reflect the incloud scavenging of IN by precipitation. Extra scalars were introduced to track the depletion in the number mixing ratio of interstitial IN by becoming immersed in cloud liquid without necessarily freezing  $(n_{X,a,\text{liq}})$  and the actual number mixing ratio of immersed IN  $(n_{X,\text{imm}})$ . The cut off size for immersed and interstitial IN size distributions is determined by  $(n_{X,a,\text{liq}})$  and mixing ratio of aerosol in group  $X(Q_X)$ . To include the heterogeneous freezing of raindrops a temporary

grid of size bins was created to discretize their size distribution. If the mass mixing ratio of each bin is  $dQ_r$ , the number of IN particles in the rain that activate in time  $\Delta t$  is given by

$$\begin{split} d(\Delta n_{\rm IN, rain}) &\approx \Delta t {\rm min} \left[ (w - v_t) \frac{\partial T}{\partial z}, 0 \right] \frac{d}{dT} \\ &\times [\exp(-\gamma_X T) - 1] \sum_X \frac{d\Omega_{X, {\rm rain}}}{\omega_{X, 1, *}}. \end{split} \tag{E1}$$

For a given raindrop size bin  $d\Omega_{X,\mathrm{rain}} = \Omega_{X,\mathrm{rain}}(dQ_r/Q_r)$  is the surface area mixing ratio of IN within the raindrops. The fall velocity of raindrops is given by  $v_t$ , while w is the vertical air velocity.

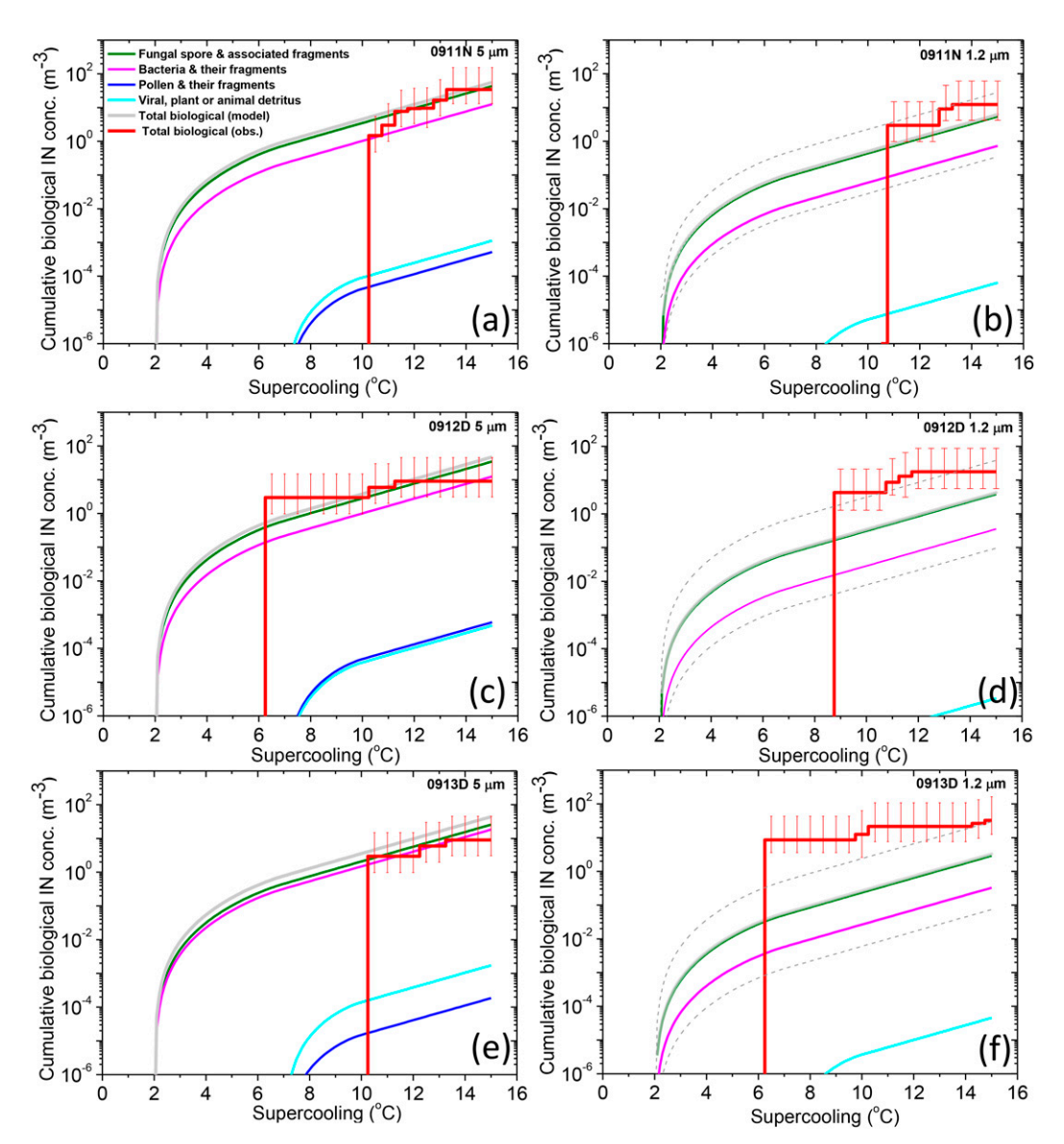


FIG. D1. Prediction of biological ice nuclei concentrations by new empirical parameterization based on the size distribution of PBAPs in 0911N, 0912D, and 0913D shown as a function of temperature for various bioaerosol species. The total biological ice nuclei concentrations from the empirical parameterization (thick black line) are compared with the observed values (thick red) from the drop freezing experiments with LINDA. For each case, the predictions based on PBAP size distribution from 5 and 1.2  $\mu$ m are shown separately. Black dotted lines in the plot of 1.2  $\mu$ m filter represent the upper and lower bounds in predicting ice nuclei concentrations due to uncertainties in collection efficiency.

We have adopted the approach followed by Phillips et al. (2008) for inside-out contact freezing. It assumes that a given IN has a freezing temperature for the contact nucleation, which is  $\Delta T_{\rm CIN} \approx 4.5^{\circ}{\rm C}$  higher than for the immersion and condensation freezing mode. The number mixing ratio of potentially active, interstitial IN activated by contact freezing  $(n_{X,\rm cn})$  is given by

$$n_{X,\text{cn}} \cong \xi(T) \left\{ \exp[-\gamma_X (T - \Delta T_{\text{CIN}})] - 1 \right\} \sum_X \frac{d\Omega_{X,\text{int}}}{\omega_{X,1,*}}. \quad (E2)$$

Here,  $\Omega_{X,\text{int}}$  is the component of  $\Omega_X$  for interstitial IN.

### REFERENCES

Adhikari, A., and Coauthors, 2009: Aerosolization of fungi, (1→3)-β-D glucan, and endotoxin from flood-affected materials collected in New Orleans homes. *Environ. Res.*, **109**, 215–224, https://doi.org/10.1016/j.envres.2008.12.010.

Amato, P., M. Joly, C. Schaupp, E. Attard, O. Möhler, C. E. Morris, Y. Brunet, and A. M. Delort, 2015: Survival and ice nucleation

- activity of bacteria as aerosols in a cloud simulation chamber. *Atmos. Chem. Phys.*, **15**, 6455–6465, https://doi.org/10.5194/acp-15-6455-2015.
- Andreae, M. O., and Coauthors, 1988: Biomass-burning emissions and associated haze layers over Amazonia. *J. Geophys. Res.*, 93, 1509–1527, https://doi.org/10.1029/JD093iD02p01509.
- —, and Coauthors, 2015: The Amazon Tall Tower Observatory (ATTO): Overview of pilot measurements on ecosystem ecology, meteorology, trace gases, and aerosols. *Atmos. Chem. Phys.*, **15**, 10 723–10 776, https://doi.org/10.5194/acp-15-10723-2015.
- Ardon-Dryer, K., and Z. Levin, 2014: Ground-based measurements of immersion freezing in the eastern Mediterranean. Atmos. Chem. Phys., 14, 5217–5231, https://doi.org/10.5194/acp-14-5217-2014.
- Ariya, P. A., J. Sun, N. A. Eltouny, E. D. Hudson, C. T. Hayes, and G. Kos, 2009: Physical and chemical characterization of bioaerosols—Implications for nucleation processes. *Int. Rev. Phys. Chem.*, 28, 1–32, https://doi.org/10.1080/01442350802597438.
- Artaxo, P., and Coauthors, 2002: Physical and chemical properties of aerosols in the wet and dry seasons in Rondônia, Amazonia. J. Geophys. Res., 107, 8081, https://doi.org/10.1029/2001JD000666.
- Barahona, D., R. E. L. West, P. Stier, S. Romakkaniemi, H. Kokkola, and A. Nenes, 2010: Comprehensively accounting for the effect of giant CCN in cloud activation parameterizations. *Atmos. Chem. Phys.*, 10, 2467–2473, https://doi.org/10.5194/acp-10-2467-2010.
- Barbosa, C. G. G., 2018: Primary biological aerosol particles at the Amazon Tall Tower Observatory: Inventory and vertical distribution. Ph.D. dissertation, Federal University of Paraná, 134 pp.
- Beydoun, H., M. Polen, and R. C. Sullivan, 2016: Effect of particle surface area on ice active site densities retrieved from droplet freezing spectra. *Atmos. Chem. Phys.*, **16**, 13359–13378, https://doi.org/10.5194/acp-16-13359-2016.
- Burrows, S. M., W. Elbert, M. G. Lawrence, and U. Pöschl, 2009: Bacteria in the global atmosphere—Part 1: Review and synthesis of literature data for different ecosystems. *Atmos. Chem. Phys.*, 9, 9263–9280, https://doi.org/10.5194/acpd-9-10777-2009.
- China, S., and Coauthors, 2016: Rupturing of biological spores as a source of secondary particles in Amazonia. *Environ. Sci. Technol.*, **50**, 12 179–12 186, https://doi.org/10.1021/acs.est.6b02896.
- Christner B. C., R. Cai, C. E. Morris, K. S. McCarter, C. M. Foreman, M. L. Skidmore, S. N. Montross, and D. C. Sand, 2008: Geographic, seasonal, and precipitation chemistry influence on the abundance and activity of biological ice nucleators in rain and snow. *Proc. Natl. Acad. Sci.*, 105, 18854–18859, https://doi.org/10.1073/pnas.0809816105.
- Conen, F., C. E. Morris, J. Leifeld, M. V. Yakutin, and C. Alewell, 2011: Biological residues define the ice nucleation properties of soil dust. *Atmos. Chem. Phys.*, 11, 9643–9648, https:// doi.org/10.5194/acp-11-9643-2011.
- Coz, E., B. Artíñano, L. M. Clark, M. Hernandez, A. L. Robinson, G. S. Casuccio, T. L. Lersch, and S. N. Pandis, 2010: Characterization of fine primary biogenic organic aerosol in an urban area in the northeastern United States. *Atmos. Environ.*, 44, 3952–3962, https://doi.org/10.1016/j.atmosenv.2010.07.007.
- Delort, A. M., M. Vaïtilingom, P. Amato, M. Sancelme, M. Parazols, G. Mailhot, P. Laj, and L. A. Deguillaume, 2010: Short overview of the microbial population in clouds: Potential roles in atmospheric chemistry and nucleation processes. *Atmos. Res.*, 98, 249–260, https://doi.org/10.1016/j.atmosres.2010.07.004.

- DeMott, P. J., and A. J. Prenni, 2010: Need for defining the numbers and sources of biological aerosols acting as ice nuclei. Atmos. Res., 44, 1944–1945, https://doi.org/10.1016/ j.atmosenv.2010.02.032.
- —, and Coauthors, 2018: The Fifth International Workshop on Ice Nucleation phase 2 (FIN-02): Laboratory intercomparison of ice nucleation measurements. *Atmos. Meas. Tech.*, **11**, 6231–6257, https://doi.org/10.5194/amt-11-6231-2018.
- Després, V., and Coauthors, 2012: Primary biological aerosol particles in the atmosphere: A review. *Tellus*, 64B, 15598, https://doi.org/10.3402/tellusb.v64i0.15598.
- Diehl, K., and S. K. Mitra, 2015: New particle-dependent parameterizations of heterogeneous freezing processes: Sensitivity studies of convective clouds with an air parcel model. *Atmos. Chem. Phys.*, 15, 12741–12763, https://doi.org/10.5194/acp-15-12741-2015.
- ——, S. Matthias-Maser, R. Jaenicke, and S. K. Mitra, 2002: The ice nucleating ability of pollen: Part II. Laboratory studies in immersion and contact freezing modes. *Atmos. Res.*, 61, 125–133, https://doi.org/10.1016/S0169-8095(01)00132-6.
- Draxler, R. R., and G. D. Rolph, 2003: HYSPLIT. NOAA Air Resources Laboratory, http://ready.arl.noaa.gov/HYSPLIT.php.
- Felgitsch, L., and Coauthors, 2018: Birch leaves and branches as a source of ice-nucleating macromolecules. *Atmos. Chem. Phys.*, **18**, 16 063–16 079, https://doi.org/10.5194/acp-18-16063-2018.
- Fröhlich-Nowoisky J., T. C. J. Hill, B. G. Pummer, G. D. Franc, and U. Pöschl, 2015: Ice nucleation activity in the widespread soil fungus *Mortierella alpina*. *Biogeosciences*, 12, 1057–1071, https://doi.org/10.5194/bg-12-1057-2015.
- Fröhlich-Nowoisky, J., and Coauthors, 2016: Bioaerosols in the Earth system: Climate, health, and ecosystem interactions. *Atmos. Res.*, 182, 346–376, https://doi.org/10.1016/j.atmosres.2016.07.018.
- Garcia, E., T. C. J. Hill, A. J. Prenni, P. J. DeMott, G. D. Franc, and S. M. Kreidenweis, 2012: Biogenic ice nuclei in boundary layer air over two U.S. High Plains agriculture regions. *J. Geophys. Res.*, **117**, D18209, https://doi.org/10.1029/2012JD018343.
- Govindarajan, A. G., and S. E. Lindow, 1988: Size of bacterial icenucleation sites measured in situ by radiation inactivation analysis. *Proc. Natl. Acad. Sci. USA*, 85, 1334–1338, https:// doi.org/10.1073/pnas.85.5.1334.
- Haga, D. I., and Coauthors, 2014: Ice nucleation by fungal spores from the classes Agaricomycetes, Ustilaginomycetes, and Eurotiomycetes, and the effect on the atmospheric transport of these spores. Atmos. Chem. Phys., 14, 8611–8630, https:// doi.org/10.5194/acp-14-8611-2014.
- Hill, T., B. F. Moffett, P. J. Demott, D. G. Georgakopoulos, W. L. Stump, and G. D. Franc, 2014: Measurement of ice nucleationactive bacteria on plants and in precipitation by quantitative PCR. Appl. Environ. Microbiol., 80, 1256–1267, https://doi.org/ 10.1128/AEM.02967-13.
- Hiron, T., and A. I. Flossmann, 2015: A study of the role of the parameterization of heterogeneous ice nucleation for the modeling of microphysics and precipitation of a convective cloud. J. Atmos. Sci., 72, 3322–3339, https://doi.org/10.1175/ JAS-D-15-0026.1.
- Holanda, B. A., and Coauthors, 2020: Influx of African biomass burning aerosol during the Amazonian dry season through layered transatlantic transport of black carbon-rich smoke. *Atmos. Chem. Phys.*, 20, 4757–4785, https://doi.org/10.5194/ acp-20-4757-2020.
- Hoose, C., and O. Möhler, 2012: Heterogeneous ice nucleation on atmospheric aerosols: A review of results from laboratory

- experiments. Atmos. Chem. Phys., **12**, 9817–9854, https://doi.org/10.5194/acp-12-9817-2012.
- —, J. E. Kristjansson, and S. M. Burrows, 2010: How important is biological ice nucleation in clouds on a global scale? *Environ. Res. Lett.*, 5, 024009, https://doi.org/10.1088/1748-9326/5/2/024009.
- Huffman, J. A., and Coauthors, 2012: Size distributions and temporal variations of biological aerosol particles in the Amazon rainforest characterized by microscopy and realtime UV-APS fluorescence techniques during AMAZE-0. Atmos. Chem. Phys., 12, 11 997–12 019, https://doi.org/ 10.5194/acp-12-11997-2012.
- —, and Coauthors, 2013: High concentrations of biological aerosol particles and ice nuclei during and after rain. *Atmos. Chem. Phys.*, **13**, 6151–6164, https://doi.org/10.5194/acp-13-6151-2013.
- Hummel, M., C. Hoose, B. Pummer, C. Schaupp, J. Fröhlich-Nowoisky, and O. Möhler, 2018: Simulating the influence of primary biological aerosol particles on clouds by heterogeneous ice nucleation. *Atmos. Chem. Phys.*, 18, 15 437–15 450, https://doi.org/10.5194/acp-18-15437-2018.
- Joly, M., P. Amato, L. Deguillaume, M. Monier, C. Hoose, and A. M. Delort, 2014: Quantification of ice nuclei active at near 0°C temperatures in low-altitude clouds at the Puy de Dôme atmospheric station. *Atmos. Chem. Phys.*, 14, 8185–8195, https://doi.org/10.5194/acp-14-8185-2014.
- Kanji, Z. A., L. A. Ladino, H. Wex, Y. Boose, M. Burkert-Kohn, D. J. Cziczo, and M. Krämer, 2017: Overview of ice nucleating particles. *Ice Formation and Evolution in Clouds* and Precipitation: Measurement and Modeling Challenges, Meteor. Monogr., No. 58, Amer. Meteor. Soc., https:// doi.org/10.1175/AMSMONOGRAPHS-D-16-0006.1.
- Klein, H., W. Haunold, U. Bundke, B. Nillius, T. Wetter, S. Schallenberg, and H. Bingemer, 2010: A new method for sampling of atmospheric ice nuclei with subsequent analysis in a static diffusion chamber. *Atmos. Res.*, 96, 218–224, https://doi.org/10.1016/j.atmosres.2009.08.002.
- Knopf, D. A., P. A. Alpert, and B. Wang, 2018: The role of organic aerosol in atmospheric ice nucleation: A review. ACS Earth Space Chem., 2, 168–202, https://doi.org/ 10.1021/acsearthspacechem.7b00120.
- Kunert, A. T., and Coauthors, 2019: Macromolecular fungal ice nuclei in Fusarium: Effects of physical and chemical processing. *Biogeosciences*, 16, 4647–4659, https://doi.org/10.5194/bg-16-4647-2019.
- Levin, Z., S. A. Yankofsky, D. Pardes, and N. Magal, 1987: Possible application of bacterial condensation freezing to artificial rainfall enhancement. *Biotechnol. Prog.*, 26, 1188–1197, https://doi.org/10.1175/1520-0450(1987)026<1188:PAOBCF>2.0.CO;2.
- Li, W., and Coauthors, 2020: Overview of primary biological aerosol particles from a Chinese boreal forest: Insight into morphology, size, and mixing state at microscopic scale. *Atmos. Res.*, 719, 137520, https://doi.org/10.1016/j.scitotenv.2020.137520.
- Lippé R., 2018: Flow virometry: A powerful tool to functionally characterize viruses. J. Virol., 92, e01765-17, https://doi.org/ 10.1128/JVI.01765-17.
- Löbs, N., and Coauthors, 2020: Aerosol measurement methods to quantify spore emissions from fungi and cryptogamic covers in the Amazon. *Atmos. Meas. Tech.*, **13**, 153–164, https://doi.org/10.5194/amt-13-153-2020.
- Martin, S. T., and Coauthors, 2010: Sources and properties of Amazonian aerosol particles. Rev. Geophys., 48, RG2002, https://doi.org/10.1029/2008RG000280.

- Matthias-Maser, S., and R. Jaenicke, 1995: The size distribution of primary biological aerosol particles with radii 0.2 mm in an urban/rural influenced region. *Atmos. Res.*, **39**, 279–286, https://doi.org/10.1016/0169-8095(95)00017-8.
- McCluskey, C. S., and Coauthors, 2018: A mesocosm double feature: Insights into the chemical makeup of marine ice nucleating particles. J. Atmos. Sci., 75, 2405–2423, https://doi.org/10.1175/JAS-D-17-0155.1.
- Moran-Zuloaga, D., and Coauthors, 2018: Long-term study on coarse mode aerosols in the Amazon rain forest with the frequent intrusion of Saharan dust plumes. *Atmos. Chem. Phys.*, **18**, 10 055–10 088, https://doi.org/10.5194/acp-18-10055-2018.
- Morris, C. E., D. C. Sands, M. Bardin, R. Jaenicke, B. Vogel, C. Leyronas, P. Ariya, and R. Psenner, 2011: Microbiology and atmospheric processes: Research challenges concerning the impact of airborne micro-organisms on the atmosphere and climate. *Biogeosciences*, 8, 17–25, https://doi.org/10.5194/bg-8-17-2011.
- —, —, C. Glaux, J. Samsatly, S. Asaad, A. R. Moukahel, F. L. T. Goncalves, and E. K. Bigg, 2013: Urediospores of rust fungi are ice nucleation active at > -10°C and harbor ice nucleation active bacteria. *Atmos. Chem. Phys.*, **13**, 4223–4233, https://doi.org/10.5194/acp-13-4223-2013.
- Murray, B. J., D. O'Sullivan, J. D. Atkinson, and M. E. Webb, 2012: Ice nucleation by particles immersed in supercooled cloud droplets. *Chem. Soc. Rev.*, 41, 6519–6554, https://doi.org/ 10.1039/c2cs35200a.
- Niemand, M., and Coauthors, 2012: A particle-surface-area-based parameterization of immersion freezing on desert dust particles. J. Atmos. Sci., 69, 3077–3092, https://doi.org/10.1175/JAS-D-11-0249.1.
- O'Sullivan, D., B. Murray, J. F. Ross, T. F. Whale, H. C. Price, J. D. Atkinson, N. S. Umo, and M. E. Webb, 2015: The relevance of nanoscale biological fragments for ice nucleation in clouds. *Sci. Rep.*, **5**, 8082, https://doi.org/10.1038/srep08082.
- Phillips, V. T. J., P. J. DeMott, and C. Andronache, 2008: An empirical parameterization of heterogeneous ice nucleation for multiple chemical species of aerosol. *J. Atmos. Sci.*, 65, 2757–2783, https://doi.org/10.1175/2007JAS2546.1.
- —, and Coauthors, 2009: Potential impacts from biological aerosols on ensembles of continental clouds simulated numerically. *Biogeosciences*, 6, 987–1014, https://doi.org/10.5194/ bg-6-987-2009.
- —, P. J. Demott, C. Andronache, K. A. Pratt, K. A. Prather, R. Subramanian, and C. Twohy, 2013: Improvements to an empirical parameterization of heterogeneous ice nucleation and its comparison with observations. *J. Atmos. Sci.*, 70, 378–409, https://doi.org/10.1175/JAS-D-12-080.1.
- Pöhlker, C., and Coauthors, 2019: Land cover and its transformation in the backward trajectory footprint region of the Amazon Tall Tower Observatory. *Atmos. Chem. Phys.*, **19**, 8425–8470, https://doi.org/10.5194/acp-19-8425-2019.
- Pöhlker, M. L., and Coauthors, 2016: Long-term observations of cloud condensation nuclei in the Amazon rain forest—Part 1: Aerosol size distribution, hygroscopicity, and new model parametrizations for CCN prediction. *Atmos. Chem. Phys.*, 16, 15 709–15 740, https://doi.org/10.5194/acp-16-15709-2016.
- ——, and Coauthors, 2018: Long-term observations of cloud condensation nuclei over the Amazon rain forest—Part 2: Variability and characteristics of biomass burning, long-range transport, and pristine rain forest aerosols. *Atmos. Chem. Phys.*, 18, 10 289–10 331, https://doi.org/10.5194/acp-18-10289-2018.

- Pöschl, U., and Coauthors, 2010: Rainforest aerosols as biogenic nuclei of clouds and precipitation in the Amazon. *Science*, 329, 1513–1516, https://doi.org/10.1126/science.1191056.
- Pouzet, G., E. Peghaire, M. Aguès, J.-L. Baray, F. Conen, and P. Amato, 2017: Atmospheric processing and variability of biological ice nucleating particles in precipitation at Opme, France. *Atmosphere*, 8, 229, https://doi.org/10.3390/atmos8110229.
- Prenni, A. J., and Coauthors, 2009: Relative roles of biogenic emissions and Saharan dust as ice nuclei in the Amazon basin. *Nat. Geosci.*, **2**, 402–405, https://doi.org/10.1038/ngeo517.
- —, and Coauthors, 2013: The impact of rain on ice nuclei populations at a forested site. *Geophys. Res. Lett.*, 40, 227–231, https://doi.org/10.1029/2012GL053953.
- Priyamvada, H., R. K. Singh, M. Akila, R. Ravikrishna, R. S. Verma, and S. S. Gunthe, 2017: Seasonal variation of the dominant allergenic fungal aerosols—One year study from southern Indian region. Sci. Rep., 7, 11171, https://doi.org/10.1038/s41598-017-11727-7.
- Pruppacher, H. R., and J. D. Klett, 1997: *Microphysics of Clouds and Precipitation*. Kluwer Academic Publishers, 954 pp.
- Pummer, B. G., H. Bauer, J. Bernardi, S. Bleicher, and H. Grothe, 2012: Suspendable macromolecules are responsible for ice nucleation activity of birch and conifer pollen. Atmos. Chem. Phys., 12, 2541–2550, https://doi.org/ 10.5194/acp-12-2541-2012.
- —, and Coauthors, 2015: Ice nucleation by water-soluble macromolecules. *Atmos. Chem. Phys.*, **15**, 4077–4091, https://doi.org/10.5194/acp-15-4077-2015.
- Richard, C., J. G. Martin, and S. Pouleur, 1996: Ice nucleation activity identified in some phytopathogenic *Fusarium* species. *Phytoprotection*, 77, 83–92, https://doi.org/10.7202/706104ar.
- Rogers, R. R., and M. K. Yau, 1989: A Short Course in Cloud Physics. 3rd ed. Butterworth-Heinemann, 304 pp.
- Schill, G. P., and Coauthors, 2020: The contribution of black carbon to global ice nucleating particle concentrations relevant to mixed-phase clouds. *Proc. Natl. Acad. Sci. USA*, 117, 22705–22711, https://doi.org/10.1073/pnas.2001674117.
- Schnell, R. C., and G. Vali, 1976: Biogenic ice nuclei: Part I. Terrestrial and marine sources. J. Atmos. Sci., 33, 1554–1564, https://doi.org/10.1175/1520-0469(1976)033<1554:BINPIT> 2.0.CO:2.
- —, and S. N. Tan-Schnell, 1982: Kenyan tea litter: A source of ice nuclei. Tellus, 34, 92–95, https://doi.org/10.3402/tellusa.v34i1.10791.
- Schrod, J., A. Danielczok, D. Weber, M. Ebert, E. S. Thomson, and H. G. Bingemer, 2016: Re-evaluating the Frankfurt isothermal static diffusion chamber for ice nucleation. *Atmos. Meas. Tech.*, **9**, 1313–1324, https://doi.org/10.5194/amt-9-1313-2016.
- —, and Coauthors, 2020: Long-term deposition and condensation ice-nucleating particle measurements from four stations across the globe. *Atmos. Chem. Phys.*, 20, 15983–16006, https://doi.org/10.5194/acp-20-15983-2020.
- Sesartic, A., U. Lohmann, and T. Storelvmo, 2012: Bacteria in the ECHAM5-HAM global climate model. *Atmos. Chem. Phys.*, 12, 8645–8661, https://doi.org/10.5194/acp-12-8645-2012.
- Shi, Z., L. Shao, T. P. Jones, A. G. Whittaker, S. Lu, K. A. Berube, T. He, and R. J. Richards, 2003: Characterization of airborne individual particles collected in an urban area, a satellite city

- and a clean air area in Beijing. *Atmos. Environ.*, **37**, 4097–4108, https://doi.org/10.1016/S1352-2310(03)00531-4.
- Soo, J. C., K. Monaghan, T. Lee, M. Kashon, and M. Harper, 2016: Air sampling filtration media: Collection efficiency for respirable size-selective sampling. *Aerosol Sci. Technol.*, 50, 76–87, https://doi.org/10.1080/02786826.2015.1128525.
- Stopelli, E., F. Conen, L. Zimmermann, C. Alewell, and C. E. Morris, 2014: Freezing nucleation apparatus puts new slant on study of biological ice nucleators in precipitation. *Atmos. Meas. Tech.*, 7, 129–134, https://doi.org/10.5194/amt-7-129-2014.
- Tamer Vestlund, A., R. Al-Ashaab, S. F. Tyrrel, P. J. Longhurst, S. J. T. Pollard, and G. H. Drew, 2014: Morphological classification of bioaerosols from composting using scanning electron microscopy. Waste Manage., 34, 1101–1108, https:// doi.org/10.1016/j.wasman.2014.01.021.
- Vali, G., 1971: Quantitative evaluation of experimental results an the heterogeneous freezing nucleation of supercooled liquids. *J. Atmos. Sci.*, **28**, 402–409, https://doi.org/10.1175/1520-0469(1971)028<0402:QEOERA>2.0.CO;2.
- ——, 1994: Freezing rate due to heterogeneous nucleation. *J. Atmos. Sci.*, **51**, 1843–1856, https://doi.org/10.1175/1520-0469(1994) 051<1843:FRDTHN>2.0.CO:2.
- ——, P. J. DeMott, O. Möhler, and T. F. Whale, 2015: A proposal for ice nucleation terminology. *Atmos. Chem. Phys.*, 15, 10263–10270, https://doi.org/10.5194/acp-15-10263-2015.
- Valsan, A. E., and Coauthors, 2015: Morphological characteristics of bioaerosols from contrasting locations in southern tropical India—A case study. *Atmos. Environ.*, 122, 321–331, https://doi.org/10.1016/j.atmosenv.2015.09.071.
- —, R. Ravikrishna, C. V. Biju, C. Pöhlker, V. R. Després, J. A. Huffman, U. Pöschl, and S. S. Gunthe, 2016: Fluorescent biological aerosol particle measurements at a tropical high-altitude site in southern India during the southwest monsoon season. *Atmos. Chem. Phys.*, 16, 9805–9830, https://doi.org/10.5194/acp-16-9805-2016.
- Whitehead, J. D., and Coauthors, 2016: Biogenic cloud nuclei in the central Amazon during the transition from wet to dry season. *Atmos. Chem. Phys.*, **16**, 9727–9743, https://doi.org/10.5194/acp-16-9727-2016.
- Wilson, T., and Coauthors, 2015: A marine biogenic source of atmospheric ice-nucleating particles. *Nature*, 525, 234–238, https://doi.org/10.1038/nature14986.
- Wittmaack, K., 2005: Brochosomes produced by leafhoppers—A widely unknown, yet highly abundant species of bioaerosols in ambient air. *Atmos. Environ.*, **39**, 1173–1180, https://doi.org/10.1016/j.atmosenv.2004.11.003.
- Wu, L., and Coauthors, 2019: Single-particle characterization of aerosols collected at a remote site in the Amazonian rainforest and an urban site in Manaus, Brazil. Atmos. Chem. Phys., 19, 1221–1240, https://doi.org/10.5194/acp-19-1221-2019.
- Xia, Y., F. Conen, and C. Alewell, 2013: Total bacterial number concentration in free tropospheric air above the Alps. *Aerobiologia*, 29, 153–159, https://doi.org/10.1007/s10453-012-9259-x.
- Xu, F., and L. P. R. de Craene, 2013: Pollen morphology and ultrastructure of selected species from Annonaceae. *Plant Syst. Evol.*, 299, 11–24, https://doi.org/10.1007/s00606-012-0698-1.